Algorithmic augmentation in the pseudopotential-based lattice Boltzmann method for simulating the pool boiling phenomenon with high-density ratio

Aritra Mukherjee ◉,* Dipankar N. Basu ◉,† and Pranab K. Mondal ◉‡

Department of Mechanical Engineering, Indian Institute of Technology Guwahati, Guwahati 781039, India

The pseudopotential-based lattice Boltzmann method (LBM), despite enormous potential in facilitating natural development and migration of interfaces during multiphase simulation, remains restricted to low-density ratios, owing to inherent thermodynamic inconsistency. The present paper focuses on augmenting the basic algorithm by enhancing the isotropy of the discrete equation and thermodynamic consistency of the overall formulation, to expedite simulation of pool boiling at higher-density ratios. Accordingly, modification is suggested in the discrete form of the updated interparticle interaction term, by expanding the discretization to the eighth order. The proposed amendment is successful in substantially reducing the spurious velocity in the vicinity of a static droplet, while allowing stable simulation at a much higher-density ratio under identical conditions, which is a noteworthy improvement over existing Single Relaxation Time (SRT)-LBM algorithms. Various pool boiling scenarios have been explored for a reduced temperature of 0.75, which itself is significantly lower than reported in comparable literature, in both rectangular and cylindrical domains, and also with micro- and distributed heaters. All three regimes of pool boiling have aptly been captured with both plain and structured heaters, allowing the development of the boiling curve. The predicted value of critical heat flux for the plain heater agrees with Zuber correlation within 10%, illustrating both quantitative and qualitative capability of the proposed algorithm.

I. INTRODUCTION

The phenomenon of boiling, while being ubiquitous in nature, offers a pivotal contribution in numerous industrial and domestic activities. It facilitates a substantially enhanced heat transfer rate, alongside rather uniform temperature distribution over the heated surface with lesser fluid volume. Flow boiling, involving forced bulk motion of a multiphase mixture, has greater relevance to numerous commercial appliances, encompassing gigantic power boilers to micro heat sinks. However, pool boiling, characterized by buoyancy-induced motion in an initially quiescent liquid column, has enticed researchers more by virtue of the rich hydrodynamics involved. Wide disparity in thermal-hydraulic characteristics across various flow regimes [1] and considerable variation in the strength of thermal communication along the heated surface have fascinated scientists across generations right from the conceptualization of the boiling curve by Nukiyama (reproduced in [2]). While the role of experimentation remains paramount in visual appraisal and global evaluation of pool boiling, a comprehensive local depiction solely through experiments remains elusive owing to the limitations of measuring tools, involvement of broad parametric ranges, and transitory nature of the event itself. Accordingly the intricate process of bubble nucleation and intriguing interfacial interactions

postdeparture continue to be confined only to the empirical level based on the experimental database. That provides an excellent opportunity for numerical exploration and consequently several computational methods have been proposed, in the field of multiphase flow in general and boiling in particular [3,4], over the last few decades, with varied degrees of success, ranging from macroscopic to molecular scales.

Son and Dhir [5] were apparently the first ones to propose a level-set method for simulating boiling, whereas Welch and Wilson [6] introduced the volume-of-fluid approach. Multiple efforts are available in literature to design a favorable amalgamation of the above two [7,8]. All such endeavors, however, suffer from one common constraint regarding the requirement of a preexisting vapor embryo or film for initiating any phase-change procedure, thereby limiting their applicability while simulating the onset of nucleate boiling or transition to film boiling. That necessitates the adoption of a computational framework unrestrained by the continuum hypothesis, and the mesoscopic approach gains prominence in this particular context. Development of the lattice Boltzmann method (LBM) is one of the most significant evolutions in the terrain of computational fluid dynamics in the present millennium. Acquiring origin from Boltzmann's kinetic molecular dynamics, it uses the discretized form of Boltzmann's equation, which is more fundamental, while avoiding any Poisson equation for pressure and being easily amenable to massive parallelization [9,10]. Notable success of LBM in incompressible single-phase systems has encouraged development of several multiphase LB algorithms, with the free-energy model [11] and pseudopotential-based Shan-Chen model [12–16] being the most referenced ones. While the former is

---

*ammaritra@gmail.com, m.aritra@iitg.ac.in
†https://www.iitg.ac.in/dnbasu/; dipankar.n.basu@gmail.com, dnbasu@iitg.ac.in
‡https://www.iitg.ac.in/pranabm/; mail2pranab@gmail.com, pranabm@iitg.ac.in

thermodynamically consistent, it follows a "top-down" approach by defining a macroscopic free energy, thereby deviating from the LB philosophy itself. Consequently the multiphase community has favored the latter approach more, which adopts a "bottom-up" procedure by postulating interparticle interaction through pseudopotentials, as detailed later. The Shan-Chen (SC) model allows natural development and migration of interfaces, accordingly evading the need of any explicit interface-tracking algorithm, as well as assumption of initial nucleus.

Thermodynamic inconsistency is one of the issues for the SC model, which has enticed significant research attention. With required amendments, Gong and Cheng [17,18] were probably the first to successfully capture the bubble dynamics during nucleate pool boiling within a computational domain filled with pure quiescent liquid, and a microheater placed at the bottom wall. The imposed equation of state (EOS) alone was adequate to simulate vapor nucleation within the superheated liquid layer. Their work instigated several follow-up studies involving SC-LBM to explore the intricate thermo-hydrodynamics of nucleate pool boiling [19–23]. Pioneering effort towards numerically developing the boiling curve can be credited to Li *et al.* [21], as they implemented a wider heater and were able to reproduce all the three regimes of pool boiling. Quite a few subsequent studies are available in open literature, focusing either on phase transition on complex or structured surfaces or on exploring the influence of relevant parameters like surface wettability [22–25], which definitely helped in envisaging the thermal characteristics of the heated surface. All the quoted studies, however, are severely restricted in terms of the employed density ratios (around 10), renouncing the extension of the concerned conclusions to practical systems. Spurious velocity currents in the vicinity of the curved interface swell significantly with the increment of density ratio in such models, inducing oscillations in the temperature profile, forcing the simulation to be unstable and unreliable. Some efforts were reported to enhance the limit of density ratio suitable to SC-LBM, such as the modified discretization scheme of Shan [26], which again is restricted to isothermal flows owing to thermodynamic inconsistencies.

It is logical to recount here that other variations of multiphase LB algorithms also encounter issues while dealing with larger density ratios, similar to SC-LBM. The free-energy-based isothermal approach of Wagner [27] suffers from insufficient Gallilean invariance, originating from the incorporation of the pressure tensor using the equilibrium distribution function and noncompatible discretization of the driving forces. Similar concerns were also raised regarding the model proposed by He *et al.* [28], employing a mesoscopic analog of the Cahn-Hilliard interface tracking equation. Mohammadi-Shad and Lee [29] aimed to revamp their formulation by introducing a sharp-interface energy equation and a source term in the pressure evolution equation to replicate the interfacial mass flow rate. Their phase-field approach, however, is not capable of stimulating phase change spontaneously, necessitating the assumption of an interface in the form of an initial bubble or film, and error in mass convergence was reported to depend on the imposed interface thickness. An older version of the pseudopotential-based thermal LBM was explored by Seta and Okui [30]. But, by their

own admission, they were restricted to an unrealistically small density ratio of 4, owing to the inherent thermodynamic inconsistency of their formulation. A more innovative approach was proposed by Tanaka *et al.* [31], as they introduced a new distribution function to add an evolution equation for pressure in their isothermal phase-field model. However, the explicit solution requirement for the pressure field makes their algorithm computationally expensive and also deviate from the strictly local nature of LB collision. The recent study of Fei *et al.* [32] is also worth mentioning here, where they combined the cascaded LBM with the SC pseudopotential method in a hybrid framework, to simulate all three regimes of pool boiling for a density ratio of 17.5. Collision operation was performed in moment space, while retaining the basic structure of the pseudopotential force. They were able to efficaciously reproduce both isothermal multiphase flow and pool boiling, albeit with the apprehension of possible challenges in dealing with higher-density ratios owing to greater resource requirement and augmentation of spurious velocities around the interface.

It is, therefore, quite evident that, despite enormous potential, the SC-LBM, and most of the other variations of multiphase LBM, have primarily been restricted to low-density-ratio scenarios, limiting the application in the vicinity of the critical point for any fluid. Nearly all the Single Relaxation Time (SRT)-based algorithms are restricted to $0.85T_c$ or higher [21–23,32]. Multiple Relaxation Time (MRT)-centered approaches have breached that temperature barrier [20], albeit at the expense of substantially greater computational resources and added intricacy. That provides the necessary impetus for the present paper, where the sole focus is on augmenting the SRT-SC-LBM algorithm to enhance the span of the density ratio for pool boiling predictions. Accordingly, the isothermal pseudopotential model of Shan [26] and thermal multiphase model of Gong and Cheng [33] are judiciously integrated in a SRT-LB framework to elicit the favorable features of both. The developed model can be shown to be thermodynamically consistent and can traverse to noticeably higher-density ratios compared to the existing algorithms. The capability of the model will be demonstrated through examples adhering to both Cartesian and cylindrical configurations, and for both simple and complex geometries, while exploring certain parametric effects on the boiling process.

II. BASIC SC-LBM FORMULATION

The governing equation in LBM is expressed in terms of the discrete particle distribution function $f(\mathbf{x}, \boldsymbol{\zeta}, t)$, which characterizes the population density at any specific location at a particular instant of time, and evolves with a timescale comparable with the mean collision time. For thermal LB models, it is common to follow the double distribution function approach, defining a separate energy distribution function $g(\mathbf{x}, \boldsymbol{\zeta}, t)$, which can be related to fluid temperature or internal energy.

A. Momentum conservation in LBM

The migration of the particle distribution function in the ith vectorial direction can be presented as

$$f_i(\mathbf{x} + \mathbf{c}_i \Delta t, t + \Delta t) = f_i(\mathbf{x}, t) + \Omega_i(\mathbf{x}, t) + \mathbf{F}_i(\mathbf{x}, t) \quad (1)$$
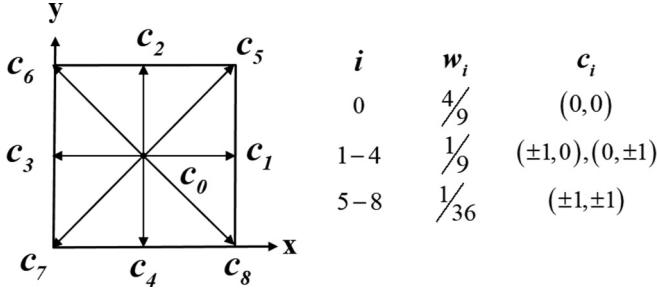
FIG. 1. Vectorial representation of the D2Q9 lattice adopted in the present paper; here $\mathbf{c}_i$ is the unit vector in the ith-velocity direction and w_i is the corresponding weight factor.

where Ω_i is the BGK collision operator [34], which relaxes the population towards the equilibrium distribution (f_i^{eq}) based on the relaxation time (τ_f) as

$$\Omega_i(\mathbf{x}, t) = -\frac{\Delta t}{\tau_f}\big[f_i(\mathbf{x}, t) - f_i^{\text{eq}}(\rho, \mathbf{u})\big]. \tag{2}$$

The relaxation time is related to the kinematic viscosity of the concerned fluid as $\nu = c_s^2(\tau_f - \frac{1}{2})\frac{\Delta x^2}{\Delta t}$. The following form of the equilibrium distribution function is adopted in the present paper:

$$f_i^{\text{eq}}(\rho, \mathbf{u}) = w_i\rho\left[1 + \frac{\mathbf{u} \cdot \mathbf{c}_i}{c_s^2} + \frac{(\mathbf{u} \cdot \mathbf{c}_i)^2}{2c_s^4} - \frac{\mathbf{u} \cdot \mathbf{u}}{2c_s^2}\right]. \tag{3}$$

Here w_i is the weight factor in the ith direction and $\mathbf{c}_i$ is the corresponding velocity vector. The D2Q9 lattice is embraced here, the schematic representation of which is shown in Fig. 1, along with the details of velocity sets and weight factors. Here $c_s = \mathbf{c}/\sqrt{3}$ is the acoustic speed of the lattice, with $\mathbf{c} = \Delta x/\Delta t$ being the lattice velocity, and Δx and Δt being selected grid spacing and time step, respectively.

The macroscopic density can be recovered from the distribution function by taking the velocity moment as

$$\rho(\mathbf{x}, t) = \sum_i f_i(\mathbf{x}, t). \tag{4}$$

The component of the body force in the ith direction $\mathbf{F}_i$ appearing in Eq. (1) is estimated following the exact difference method proposed by Kupershtokh and Medvedev [35]:

$$\mathbf{F}_i(\mathbf{x}, t) = f_i^{\text{eq}}(\rho(\mathbf{x}, t), \mathbf{u}^{\text{eq}} + \Delta\mathbf{u}) - f_i^{\text{eq}}(\rho(\mathbf{x}, t), \mathbf{u}^{\text{eq}}) \tag{5}$$

where $\Delta\mathbf{u} = \mathbf{F}\Delta t/\rho$ and $\mathbf{u}^{\text{eq}}$ is the equilibrium velocity defined as

$$\mathbf{u}^{\text{eq}}(\mathbf{x}, t) = \sum_i f_i(\mathbf{x}, t)\mathbf{c}_i. \tag{6}$$

The actual fluid velocity differs from equilibrium velocity, as it is defined as

$$\mathbf{u}(\mathbf{x}, t) = \mathbf{u}^{\text{eq}}(\mathbf{x}, t) + \frac{\mathbf{F}(\mathbf{x}, t)\tau_f\Delta t}{2\rho(\mathbf{x}, t)}. \tag{7}$$

The body force $\mathbf{F}$ is composed of the interparticle interaction force or the so-called Shan-Chen force ($\mathbf{F}^{\text{SC}}$), surface wettability force ($\mathbf{F}^{\text{wet}}$), and imposed external forces ($\mathbf{F}^{\text{ext}}$). Gravity is the sole external force field under consideration here, which has a pivotal role on bubble departure during nucleate boiling,

and the resultant buoyancy effect can be introduced following Kang *et al.* [36] as

$$\mathbf{F}^{\text{ext}}(\mathbf{x}, t) = \mathbf{g}\left\{1 - \frac{\rho_{\text{avg}}(t)}{\rho(\mathbf{x}, t)}\right\} \tag{8}$$

with $\rho_{\text{avg}}(t)$ and $\mathbf{g}$, respectively, being the instantaneous fluid density averaged over the entire computational domain and the gravitational acceleration.

B. Standard pseudopotential model

As already mentioned, the concept of employing a pseudopotential function for comprehending the interparticle interaction force was first introduced by Shan and Chen [13]. The original form of the SC force was the following:

$$\mathbf{F}^{\text{SC}}(\mathbf{x}, t) = -G_{\text{SC}}\psi(\mathbf{x}, t)\sum_i w(|\mathbf{c}_i|)\psi(\mathbf{x} + \mathbf{c}_i\Delta t, t)\mathbf{c}_i\Delta t \tag{9}$$

where $\psi(\mathbf{x})$ is known as the pseudopotential function, estimated from the nodal densities at lattice scale, and the factor G_{SC} controls the strength of the interaction force. For the adopted D2Q9 lattice structure, $w(|\mathbf{c}_i|)$ is specified as

$$w(|\mathbf{c}_i|) = \begin{cases} w_1 & \text{if } |\mathbf{c}_i| = \mathbf{c} \\ w_2 & \text{if } |\mathbf{c}_i| = \sqrt{2}\mathbf{c} \\ 0 & \text{otherwise} \end{cases} \tag{10}$$

with the constraint of $w_1 = 4w_2$ emanating from the weight factors of the concerned velocity space [9] shown in Fig. 1.

The most lucrative feature of SC-LBM is the spontaneous phase separation inherent to the algorithm and the same is realized through a non-ideal-gas EOS. The traditional form of SC-EOS can be obtained by expanding $\mathbf{F}^{\text{SC}}$ and comparing it with the anisotropic pressure tensor of the macroscopic momentum conservation equation [15]:

$$p(\mathbf{x}, t) = c_s^2\rho(\mathbf{x}, t) + \frac{G_{\text{SC}}\Delta t^2}{2}\psi^2(\mathbf{x}, t). \tag{11}$$

The EOS must ensure simultaneous existence of two phases with distinct characteristic densities within a multiphase mixture at specified pressure and temperature, and the concerned densities ought to comply with the Maxwell area construction rule [37]. The absence of temperature in Eq. (11), however, places a serious restriction, engendering thermodynamic inconsistency. To address the same, Yuan and Schaefer [37] devised a new method of introducing a more realistic EOS while estimating the pseudopotential function as

$$\psi(\mathbf{x}, t) = \sqrt{\frac{2[p(\mathbf{x}, t) - c_s^2\rho(\mathbf{x}, t)]}{G_c}}. \tag{12}$$

Here the pressure (p) can be replaced by any realistic equation of state, ensuring liquid-vapor coexistence. The Peng-Robinson EOS (PR-EOS) provides very precise estimation for a wide variety of fluids, particularly near the critical point [17,38], and the same is embraced in the present paper:

$$p(\mathbf{x}, t) = \frac{\rho RT}{1 - b\rho} - \frac{a\alpha(T)\rho^2}{1 + 2b\rho - b^2\rho^2} \tag{13}$$

where

$$\sqrt{\alpha(T)} = 1 + \kappa(1 - \sqrt{T_R}),$$

$$\kappa = 0.374\,64 + 1.542\,26\omega - 0.269\,92\omega^2,$$

$$a = 0.457\,24\big(R^2 T_c^2 / p_c\big), \quad b = 0.0778(RT_c / p_c).$$

Here both ρ and T refer to the instantaneous nodal values, ω is a fluid-dependent acentric factor, and magnitudes of the constants a and b are taken to be 2/49 and 2/21 following Yuan and Schaefer [37]. The lattice-level value for the universal gas constant is set to be 1, and all the reduced properties (marked by subscript R) are calculated accordingly adhering to the derivative constraint.

In order to ensure a direct correspondence between the macro- and lattice scale, the principle of corresponding states must be conformed to, which demands the equality of the reduced properties across all scales. Accordingly the following equalities are enforced in the present model:

$$\rho_R = \frac{\rho^{\text{LB}}}{\rho_c^{\text{LB}}} = \frac{\rho^{\text{real}}}{\rho_c^{\text{real}}}, \quad p_R = \frac{p^{\text{LB}}}{p_c^{\text{LB}}} = \frac{p^{\text{real}}}{p_c^{\text{real}}}, \quad T_R = \frac{T^{\text{LB}}}{T_c^{\text{LB}}} = \frac{T^{\text{real}}}{T_c^{\text{real}}}.$$

(14)

By incorporating the realistic EOS, Yuan and Schaefer [37] were able to demonstrate substantial improvement in the thermodynamic consistency of the SC-LBM over a reasonably wide temperature range. Outside that range, however, the phasic densities obtained from the EOS fail to match with the analytical values, thereby limiting the regime of applicability. Predictions employing the PR-EOS start to deviate from the Maxwell construction curve for $T_R \leqslant 0.9$. Gong and Cheng [17,33] proposed the following amended form of the interparticle interaction force to enhance the thermodynamic consistency over a wider range, which is logically similar to the formulation recommended by Kupershtokh *et al.* [39]:

$$\mathbf{F}^{\text{SC}}(\mathbf{x}, t)$$

$$= -G_{\text{SC}} \sum_i w(|\mathbf{c}_i|) \begin{bmatrix} \beta\psi(\mathbf{x}, t)\psi(\mathbf{x} + \mathbf{c}_i\Delta t, t) \\ + \frac{1}{2}(1 - \beta)\psi^2(\mathbf{x} + \mathbf{c}_i\Delta t, t) \end{bmatrix}\mathbf{c}_i\Delta t$$

(15)

where β is a weighting factor associated with the concerned EOS. The optimum value corresponding to the PR-EOS is reported to be 1.16 [33].

The surface wettability force can also be incorporated through the pseudopotential function. A rather simple approach was proposed by Benzi *et al.* [40] involving a single-component multiphase mixture and solid wall as

$$\mathbf{F}^{\text{wet}}(\mathbf{x}, t) = -G_{\text{wet}}\psi(\mathbf{x}, t) \sum_i w_i\psi(\rho_w)S_{\text{ind}}(\mathbf{x} + \mathbf{c}_i\Delta t)\mathbf{c}_i\Delta t.$$

(16)

Here the false wall density ρ_w is representative of the desired contact angle and the indicator function S_{ind} identifies a node as the solid or fluid one. It assumes a value of 1 at the solid node and zero at the fluid node, consequently helping to estimate the adhesion force only at the solid surface.

C. Energy conservation in LBM

As mentioned earlier, a second distribution function is introduced to designate the thermal field, and the concerned

evolution equation can be represented as

$$g_i(\mathbf{x} + \mathbf{c}_i\Delta t, t + \Delta t) = g_i(\mathbf{x}, t) - \frac{\Delta t}{\tau_g}\big[g_i(\mathbf{x}, t) - g_i^{\text{eq}}(\rho, \mathbf{u}, T)\big]$$

$$+ w_i\Delta t\,\Phi(\mathbf{x}, t)$$

(17)

where Φ is the source term associated primarily with the latent heat transfer and the relaxation parameter (τ_g) is related to the macroscopic thermal diffusivity as $\alpha = c_s^2(\tau_g - \frac{1}{2})\frac{\Delta x^2}{\Delta t}$. The lattice-level temperature is defined as

$$T(\mathbf{x}, t) = \sum_i g_i(\mathbf{x}, t)$$

(18)

and the equilibrium form of the thermal distribution function is selected to be

$$g_i^{\text{eq}}(\rho, \mathbf{u}, T) = w_i T\left[1 + \frac{\mathbf{u} \cdot \mathbf{c}_i}{c_s^2} + \frac{(\mathbf{u} \cdot \mathbf{c}_i)^2}{2c_s^4} - \frac{\mathbf{u} \cdot \mathbf{u}}{2c_s^2}\right]. \quad (19)$$

Relevant properties like thermal conductivity and viscosity at the fluid-vapor interface are estimated employing a linear interpolation, which helps avoiding steep property gradients at the interface, resulting in a diffused-interface representation:

$$\phi(\mathbf{x}, t) = \phi_{\text{liq}}\frac{\rho(\mathbf{x}, t) - \rho_{\text{vap}}}{\rho_{\text{liq}} - \rho_{\text{vap}}} + \phi_{\text{vap}}\frac{\rho_{\text{liq}} - \rho(\mathbf{x}, t)}{\rho_{\text{liq}} - \rho_{\text{vap}}}. \quad (20)$$

Proper lattice-scale interpretation of the source term is very crucial to ensure accuracy of the solution. Using the macroscopic energy equation and thermodynamic $T\,ds$ relations, the following expansion for the source term was proposed by Házi and Márkus [41]:

$$\Phi(\mathbf{x}, t) = T\left[\frac{1}{\rho^2 c_v}\left(\frac{\partial p}{\partial T}\right)_\rho\frac{d\rho}{dt} + \nabla \cdot \mathbf{u}\right] \quad (21)$$

where $(\partial p/\partial T)_\rho$ can be accessed from the corresponding EOS. It can, however, be quite inconvenient from a numerical implementation perspective to deal with the temporal density gradient, while being computationally expensive, which motivated Gong and Cheng [17] to suggest an alternate rendition by integrating with the continuity equation as

$$\Phi(\mathbf{x}, t) = T\left[1 - \frac{1}{\rho c_v}\left(\frac{\partial p}{\partial T}\right)_\rho\right]\nabla \cdot \mathbf{u}. \quad (22)$$

The second-order central difference scheme is employed in the present paper to maintain consistency with the accuracy level of the fundamental LBM. The conjugation of momentum and thermal LB models, armed with the pseudopotential scheme, can simulate the phase-change process with reasonable veracity [17,18].

III. PROPOSED AMENDMENTS IN THE SC-LBM FRAMEWORK

Despite successful conceptualization of pool boiling in the above SC-LBM framework, applicability of nearly all the available models is restricted only in the neighborhood of the critical point, owing to their failure with higher liquid-to-vapor density ratios. Available multiphase LB algorithms are numerically unstable in such cases, incapable of locating the interface with precision. It is imperative to identify the rationale behind such shortfall, before an appropriate solution can be devised, which has motivated several research efforts
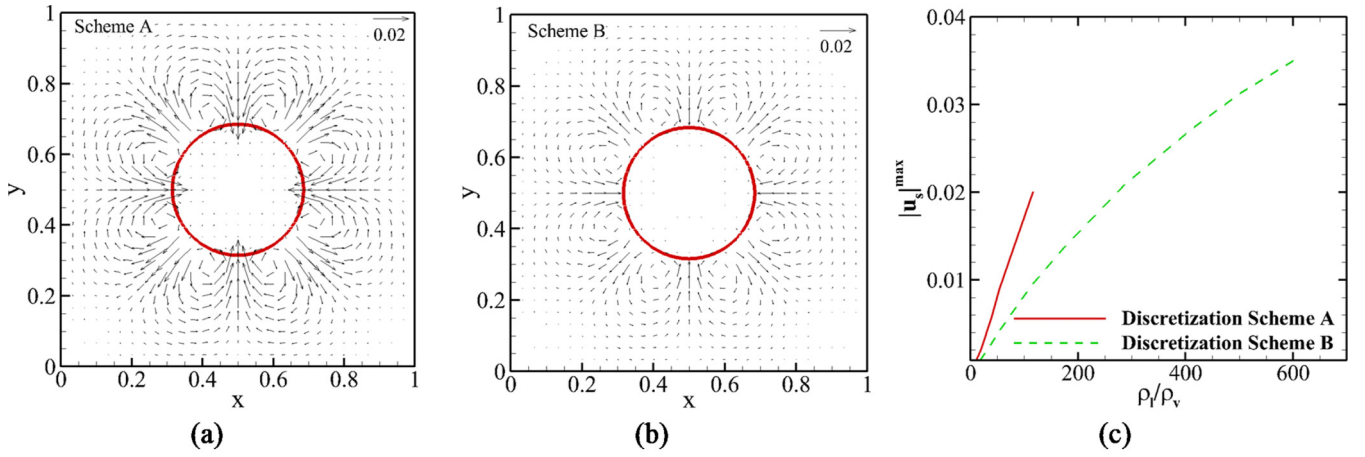
FIG. 2. Appearance of spurious velocity currents around a static liquid droplet being stabilized in a periodic domain at $T_R = 0.73$, following (a) discretization scheme A and (b) discretization scheme B, and (c) variation of maximum false velocity with density ratio following both schemes. Proposed scheme B offers substantial suppression in spurious velocity, while also enabling simulation at much higher-density ratios.

exploring a possible remedy [26,42,43]. The existence of spurious velocity currents in the vicinity of the curved interface separating the coexisting phases was identified as one of the principal contributors, which can be demonstrated through the standard static droplet problem. When such a liquid droplet is suspended in a quiescent bulk vapor field at the absence of any body force, steady-state velocity at every node should be zero for a periodic domain. However, as illustrated in Fig. 2(a), small velocity vectors exist over the complete domain, with increasingly greater magnitude as the interface is approached. Insufficient isotropy of the discretized form of the SC force term has been earmarked as the principal contributor to such spurious velocities [26,42], which gets augmented at higher-density ratios. Spurious velocity currents around the interface also induce localized fluctuations in fluid temperature, leading to capricious predictions and numerical instability at higher-density ratios.

In an attempt to trace the concerned genesis, the right-hand side of the SC force term present in Eq. (9) is expanded to the tenth order to yield

$$
\begin{aligned}
&\mathbf{F}^{SC}(\mathbf{x}, t) \\
&= -G_{SC}\psi(\mathbf{x}, t)\Delta t
\left\{
\begin{array}{c}
E_{ij}^{(2)}\partial_j\psi + \frac{1}{3!}E_{ijkl}^{(4)}\partial_{jkl}\psi \\
+ \frac{1}{5!}E_{ijklmn}^{(6)}\partial_{jklmn}\psi \\
+ \frac{1}{7!}E_{ijklmnpq}^{(8)}\partial_{jklmnpq}\psi \\
+ \frac{1}{9!}E_{ijklmnpqrs}^{(10)}\partial_{jklmnpqrs}\psi + \cdots
\end{array}
\right\}
\end{aligned}
\tag{23}
$$

where

$$
E^{(n)} = E_{i_1 i_2 i_3 \cdots i_n}^{(n)} = \sum_i w(|\mathbf{c}_i|)c_{i_1}c_{i_2}c_{i_3}\cdots c_{i_n}.
$$

Odd-order tensorial terms are absent in Eq. (23), as they must reduce to zero to ensure sufficient rotational isotropy of the lattice structure and involved velocity sets [42], which can

mathematically be summarized as

$$
E^{(2n+1)} = E_{i_1 i_2 i_3 \cdots i_n}^{(2n+1)} = \sum_i w(|\mathbf{c}_i|)c_{i_1}c_{i_2}c_{i_3}\cdots c_{i_n} = 0 \; n \geqslant 0.
\tag{24}
$$

As explained by Shan [26], truncating the discretized form of the SC force beyond the fourth-order term $E^{(4)}$ in Eq. (23) recognizes contributions only from the neighboring nodes
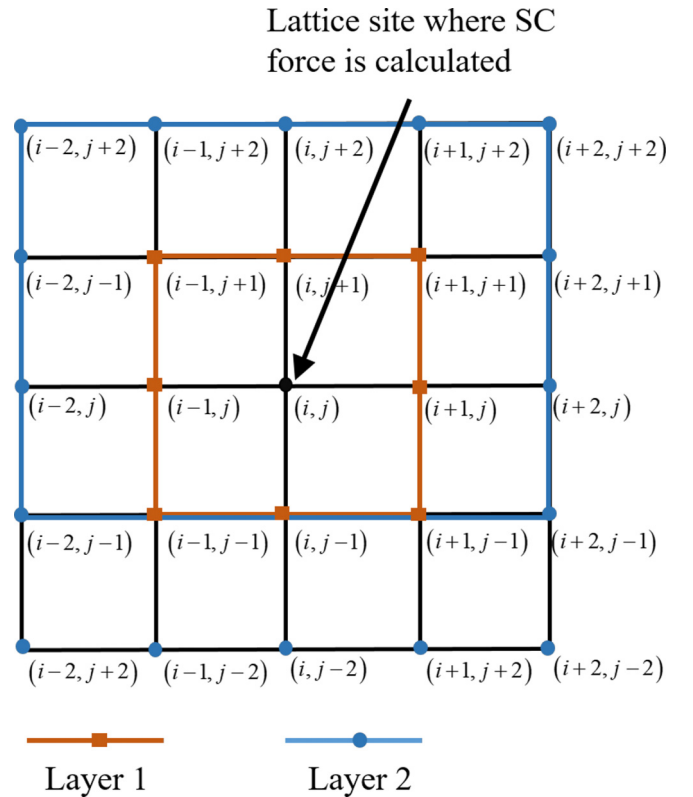

FIG. 3. Two layers of neighboring nodes considered during the proposed discretization scheme. Layer 1 involves the eight immediate neighbors and layer 2 includes the 16 next neighbors, resulting in a 25-point discretization scheme.

(layer 1 from Fig. 3), allowing $E^{(6)}$ to primarily determine the extent of the intruded anisotropy. In order to enhance the isotropy, it is imperative to include the higher-order terms, which is expected to reduce spurious velocity currents at the interface, consequently reinforcing numerical stability.

With the aim being simultaneous enhancement of isotropy of the discrete equations and thermodynamic consistency of the overall SC-LBM formulation, the present paper proposes a merger of the updated interparticle interaction force hypothesized by Gong and Cheng [33] [Eq. (15)], with the above postulate of Shan [26], by extending the discretization to $E^{(8)}$, which embodies the second layer of the neighboring nodes (layer 2 of Fig. 3) into evaluation as well. Accordingly the following is the proposed form of the updated SC force:

$$
\begin{aligned}
\mathbf{F}^{SC}(\mathbf{x}, t) = & -G_{SC}\beta\psi(\mathbf{x}, t)\Delta t \left[\begin{array}{c} lE_{ij}^{(2)}\partial_j\psi(\mathbf{x}+\mathbf{c}_i\Delta t, t) + \frac{1}{3!}E_{ijkl}^{(4)}\partial_{jkl}\psi(\mathbf{x}+\mathbf{c}_i\Delta t, t) \\ +\frac{1}{5!}E_{ijklmn}^{(6)}\partial_{jklmn}\psi(\mathbf{x}+\mathbf{c}_i\Delta t, t) + \frac{1}{7!}E_{ijklmnpq}^{(8)}\partial_{jklmnpq}\psi(\mathbf{x}+\mathbf{c}_i\Delta t, t) \end{array} \right] \\
& -G_{SC}\frac{1-\beta}{2}\Delta t \left[\begin{array}{c} lE_{ij}^{(2)}\partial_j\psi^2(\mathbf{x}+\mathbf{c}_i\Delta t, t) + \frac{1}{3!}E_{ijkl}^{(4)}\partial_{jkl}\psi^2(\mathbf{x}+\mathbf{c}_i\Delta t, t) \\ +\frac{1}{5!}E_{ijklmn}^{(6)}\partial_{jklmn}\psi^2(\mathbf{x}+\mathbf{c}_i\Delta t, t) + \frac{1}{7!}E_{ijklmnpq}^{(8)}\partial_{jklmnpq}\psi^2(\mathbf{x}+\mathbf{c}_i\Delta t, t) \end{array} \right] + O(\partial^9). \quad (25)
\end{aligned}
$$

The discretized versions of the modified SC force are detailed in the Appendix. The anisotropy in the proposed scheme is expected to stem from the corresponding tenth-order term, which must have a much smaller influence in comparison to the same in an earlier model, thereby promising the use of the modified SC-LBM algorithm to higher-density ratios. The lack of sufficient number of neighbors around the boundary nodes, however, forces us to revert back to Eq. (15) solely for them. To substantiate the enhanced isotropy of the proposed scheme, the present algorithm needs to be analyzed for a variety of scenarios involving pool boiling, and a comprehensive report for the same is presented in the next section.

IV. RESULTS AND DISCUSSION

As has been repeatedly stressed, the objective of the present paper is to devise an improved SC-LBM algorithm capable of simulating pool boiling scenarios involving higher-density ratios. It is, therefore, essential to test the proposed model for various simple and complex geometries. Before embarking on such case studies, an attempt is made to envisage the extent of improvements possible with the current framework by comparing its output with the same from existing ones, and the static droplet problem quoted earlier is selected accordingly.

A. Improvement over the existing model

Insufficient isotropy of the existing algorithms produces false velocity currents near the curved interface during multiphase simulations, yielding nonzero velocity magnitude even in the vicinity of a static droplet, as already demonstrated in Fig. 2(a). Here simulation is performed by initiating a droplet inside a periodic domain and continuing the numerical procedure until the completion of natural phase separation. False velocity currents are clearly visible in the figure, with an enhanced level of spuriousness close to the curved interface, gradually diminishing with increasing distance from the same. Formation of small local vortices is also evident. The magnitude of such spurious velocity steeply rises with the density ratio [Fig. 2(c)], making the solution unstable as the system moves away from the critical temperature.

To illustrate the improvement with the modified discretization scheme, we have performed simulations with both the methods, so that a direct comparison with the earlier model of Gong and Cheng [33] can be facilitated, and concerned observations are summarized in Fig. 2(c). Here the existing model is denoted as scheme A, whereas the updated discretization scheme [Eq. (25)] is marked as scheme B. Adopting a computational domain similar to Fang *et al.* [20], and adhering to the original formulation of Gong and Cheng [33] (scheme A), we could achieve a maximum density ratio of only about 174, which corresponds to a reduced temperature (T_R) of 0.7 for R134a, as shown in Fig. 2(b). The maximum velocity magnitude yielded by scheme B for any given density ratio is noticeably lower than the predictions from scheme A. For example, at $T_R = 0.73$, the largest amplitude of spurious velocity with scheme A is about 113% greater than the same predicted with scheme B, despite dealing with near-identical density ratios. The same can also be substantiated by visually comparing the velocity vectors depicted in Figs. 2(a) and 2(b). More importantly, stable simulation with substantially higher-density ratio is also feasible. Continuing with the simulation setup of Fang *et al.* [20] and employing the proposed SRT-LB discretization (scheme B), we have successfully computed the static droplet at a density ratio of about 600 ($T_R \approx 0.63$), which is a considerable improvement over the existing literature ($T_R \gtrsim 0.7$ in Fang *et al.* [20]). They were able to attain such temperature levels only with the MRT-LB framework [44], which is definitely more computation intensive. It is also interesting to note that, despite a higher level of spuriousness beyond a density ratio of 300, the proposed algorithm is capable of sustaining the simulation, which is an apt demonstration of the enhancement in isotropy of the discretized form.

We must, however, admit that the contribution from the second nearest neighbor in the discretized force term is not consistent with the strictly local nature of the spatial discretization in classical LBM. Any multiphase LB algorithm has a bit of nonlocality ingrained to the formulation, and consideration of the second nearest neighbor appends to that. The collision operation with both momentum and thermal distribution function, though, maintains locality, and there is no requirement of explicitly evaluating pressure unlike Tanaka *et al.* [31]. The modified scheme B requires only about 15%
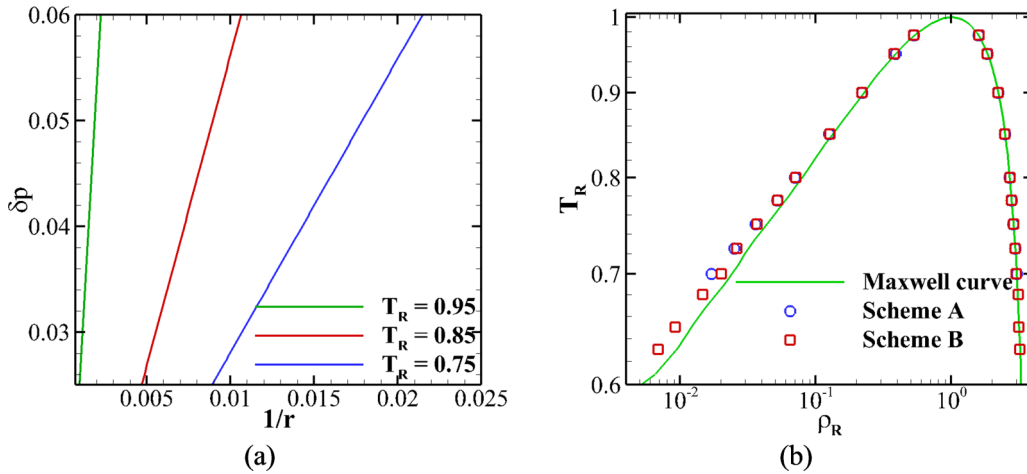
FIG. 4. Qualitative validation of the proposed algorithm: (a) The pressure differential across the interface of a static droplet exhibits a linear relationship with the reciprocal of droplet radii for three different saturation temperatures; (b) liquid and vapor coexisting densities predicted with scheme B referred to earlier demonstrate excellent conformity with the Maxwell area construction rule [37] at significantly lower reduced temperatures.

more computational time compared to scheme A while simulating pool boiling, which is quite reasonable considering the improvement achieved in suppressing the spurious velocities. The increase in computational cost with the formulation of Tanaka *et al.* [31] was substantially greater, as per their own admission. Primary contribution towards the increased time requirement with scheme B in our paper is expectedly from the SC force calculation, as the concerned CPU time rises from about 8.82 to 19.26%. Consequently, the CPU times for the momentum and thermal collision operations descend from 15.55 and 15.74%, respectively, to 13.93 and 14.11%, despite no significant change in their values. One possible penalty may, however, have to be incurred with the current scheme in terms of the enhanced complexity in parallelization owing to the nonlocality. One of the most alluring features of LBM is easy amenability to parallelization, and the intrusion of nonlocality in any multiphase LB algorithm can affect that, the SC force itself being nonlocal in nature, which can be more sizable with the inclusion of the additional layer of nodes in SC force calculation.

B. Numerical validation

The pseudopotential-based LB multiphase model does not require any specific interface-tracking algorithm, which is one of its most notable advantages. It allows natural separation of phases based on the density differential and hence it is logical to employ the traditional Laplace test for an indirect validation, which demands a precise interface conceptualization. Consequently, simulations are performed to stabilize a static liquid droplet in a vapor domain in the absence of any body force for three different reduced temperatures. Resultant variations in pressure differential across the interface ($\delta p = p_{\text{in}} - p_{\text{out}}$) are plotted with respect to the inverse of droplet radius in Fig. 4(a). A clear linear relationship is conspicuous, which is sufficient testimony towards successful diagnosis of surface tension at the interface.

As discussed earlier, another important facet to secure during any multiphase simulation is the compliance of simulated phasic densities with the analytical value obtained from the Maxwell area construction rule [37]. This is a critical constraint towards thermodynamic consistency of any multiphase LB model. Accordingly the static droplet problem is revisited over a range of reduced temperatures with both the discretization schemes, referred to earlier as scheme A and B. As presented in Fig. 4(b), both yield satisfactory reproduction of the analytical value of the saturated liquid density. There is, however, deviation on the vapor side, with scheme A noticeably veering away from the theoretical curve. The proposed scheme B is able to extend the simulation to significantly lower saturation temperature and hence much lower-density ratio, albeit at the expense of degraded accuracy for $T_r < 0.66$.

C. Problem definition

Four different geometric configurations are selected to envisage the bubble dynamics and heat transport characteristics during pool boiling with the proposed algorithm, gradually advancing from simple to complicated domains. Corresponding schematic representations are available in Fig. 5, and the associated initial and boundary conditions are delineated below.

The first test case concerns nucleate pool boiling in a rectangular domain [Fig. 5(a)], composed of 150×600 lattices. The domain is initially filled with saturated liquid maintained at $T_R = 0.75$. The synthetic refrigerant R134a is selected as the working fluid and the relevant thermophysical properties are initialized with the corresponding saturated liquid properties. PR-EOS predicts a corresponding lattice-level liquid density value of 7.68 and vapor density of 0.099, which conforms to a density ratio of about 77.6. It is considerably higher than comparable literature, where hardly any study exits for $T_R \leqslant 0.85$. As mentioned earlier, the surface wettability force is realized in Eq. (16) by tuning the false wall density at the solid node neighboring to the solid-fluid interface. Unless stated otherwise, we adhere to a fixed magnitude of $\rho_w = 4.0$, which concedes a contact angle of 56.97°. The vertical boundaries are periodic in nature, while the top
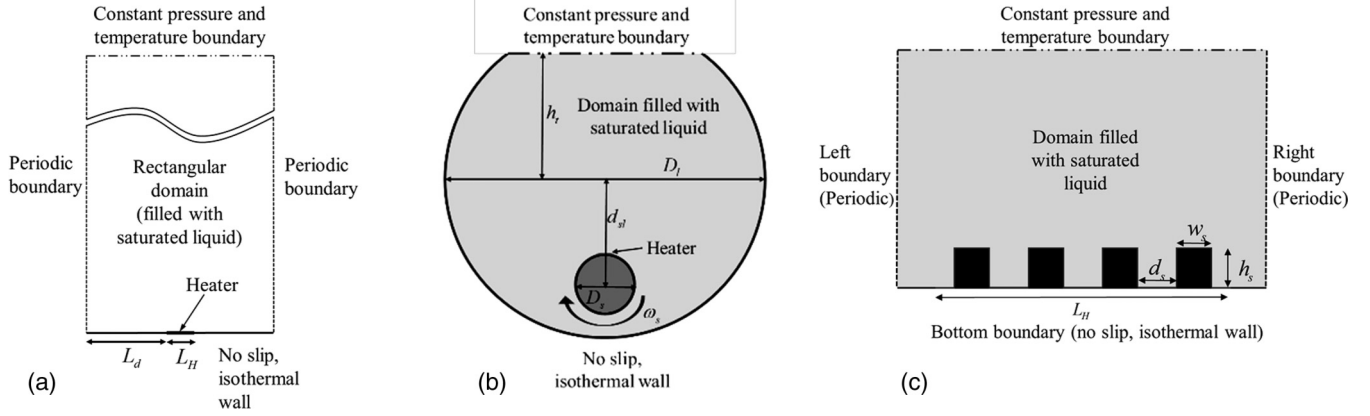
FIG. 5. Schematics of the geometric configurations considered for the present paper: (a) an open rectangular domain with a micro- or distributed heater at the bottom surface; (b) an open fluid-filled cylinder housing a noncoaxial rotating solid cylinder, which embeds a microheater at the top surface; and (c) a structured heater composed of four identical columns mounted along the bottom surface of an open rectangular domain.

boundary is identified as a free surface, characterized by saturation temperature and pressure, i.e., $T_R = 0.75$ for the present configuration. The bottom surface houses a micro-heater, portrayed by an isothermal section of five lattice unit length (l_H) with elevated temperature. The unheated part of the bottom surface is maintained at the initial temperature. All the reported computations are performed with $\beta = 1.185$ and $g = 5 \times 10^{-5}$, unless mentioned otherwise. Magnitudes of the relaxation times are obviously dependent on the prevailing fluid properties. For $T_R = 0.75$, the relaxation parameters for momentum conservation (τ_f) for liquid and vapor phases are found to be 0.75 and 1.33, respectively, while the same in relation to energy conservation (τ_g) are 0.57 and 1.47, respectively.

The second problem adopts a curvilinear geometry in the shape of a cylindrical fluid-filled container with an open face at the top, as shown in Fig. 5(b). It includes a smaller solid cylinder, with the centers of both the cylinders having a vertical offset (d_{sl}) of 100 lattice units. The diameters of the larger (D_l) and smaller (D_s) cylinders are 300 and 40 lattice units, respectively. The inner one rotates with a constant angular velocity of $\omega_s = 7.5 \times 10^{-3}$, while the other remains stationary. A microheater stretching across seven lattice units is mounted on the surface of the smaller cylinder, the surface of which is subjected to a certain controlled amount of superheat. The wall of the outer cylinder is isothermal, while the top opening is contemplated as a free surface.

The geometry of the third problem resembles the first one, with the primary difference being the incorporation of a wider heater. A plain heater of 400 lattice unit width is symmetrically emplaced on the bottom boundary of the computational domain measuring 600×800 lattice units. This configuration is modified in the fourth problem to inlay a structured heater, embodied by four identical solid columns [Fig. 5(c)]. The horizontal expanse of the heater, as well as the domain dimensions, remain unchanged. We have selected the width and height of the columns, as well as the intercolumn distance, to be the same, with $w_s = h_s = d_s = 40$ lattice units. The selected sections along the bottom wall, as well as the surface of all the columns, constitute the heater and are maintained at

the elevated temperature to instigate bubble nucleation. The initial and thermal boundary conditions stand similar to the first configuration in all the others.

It is pertinent to acknowledge that the grid structures embraced for each of the geometric configurations have been identified through systematic mesh-convergence study, which can be detailed here with the first one as example. We consider three different mesh structures, namely, 120×480, 150×600, and 180×720. Initially the rectangular domain is assumed to be filled with saturated liquid at $T_R = 0.9$, and a microheater having a width of five lattice units is placed centered at the bottom wall with $\Delta T_{\text{sup}} = 0.4$. Lattice-level magnitude of the gravitational acceleration is adjusted according to the imposed length scale, which varies with the adopted mesh structure. All the three nodal arrangements yield near-identical profiles of fluid density along the vertical centerline, which can be visualized to reveal the thickness of the diffused interface, with density changing from vaporlike to the liquidlike level as we move upward. That establishes the mesh-independent nature of the reported results, and, accordingly, we have converged on 150×600 to perform all the subsequent simulations. Similar procedure has been followed for the other three configurations as well.

To expedite direct comparison and ease of data analysis, we comply with the original definitions of the characteristic length (L_0), characteristic velocity (u_0), and characteristic time (t_0) proposed by Gong and Cheng [18] for the remainder of this paper, which are reproduced here to maintain continuity of reading:

$$l_0 = \sqrt{\frac{\sigma}{g(\rho_l - \rho_v)}}, \quad u_0 = \sqrt{gl_0}, \quad t_0 = \frac{u_0}{l_0}. \quad (26)$$

D. Rectangular domain with a microheater

The modified discretization scheme is employed first to explore the bubble dynamics during nucleation from a microheater submerged in an initially isothermal liquid pool [Fig. 5(a)]. Conventional multiphase algorithms cannot spontaneously instigate the process of heterogeneous nucleation and subsequent dynamics, owing to their ineptitude in
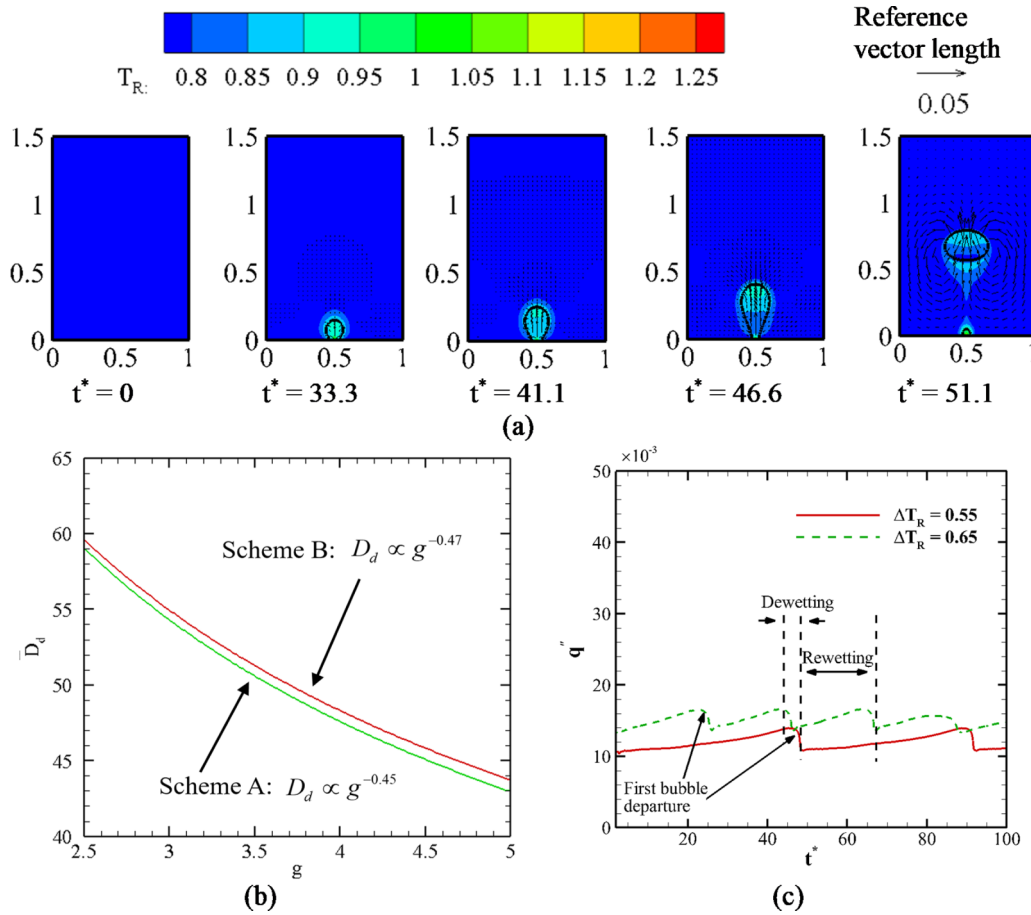
FIG. 6. Numerical characterization nucleate boiling from a microheater in an open rectangular domain: (a) snapshots of one bubble ebullition cycle presenting temperature contours, velocity vectors, and bubble contour (thick black line); (b) validation of Fritz's correlation [45] to prove that the bubble departure diameter is inversely proportional to g; and (c) temporal variation in wall heat flux for two different wall superheat values, demonstrating periodic dewetting and rewetting of the heated surface.

destabilizing the phase equilibrium, and popularly require a microbubble at the simulated nucleation site, in complete contrast to real experiments. One of the distinct merits of phase-change LB models is the nonrequirement of any artificial vapor injection or assumed nucleus. In the present algorithm, the liquid-vapor coexistence density is controlled by the adopted non-ideal-gas equation of state (PR-EOS) embedded into the modified pressure tensor. On addition of a sufficient amount of energy ($\geqslant$ enthalpy of vaporization) to the superheated liquid, PR-EOS estimates the nodal density to be equal to or less than saturated vapor density, allowing direct categorization of phases. This particular feature allows us to replicate true experimental condition into the numerical framework, stimulating nucleation on the microheater surface on addition of energy to the saturated liquid and ensuing bubble dynamics.

A series of snapshots is presented in Fig. 6(a) to demonstrate the ebullition cycle during pool boiling with the microheater, when the heater surface is subjected to a wall superheat of $\Delta T_{sup} = 0.55$. Here the time step is normalized using the characteristic time defined above ($t^* = t/t_0$). The first picture in Fig. 6(a) depicts the initial status of the domain, where it is filled with quiescent liquid at saturation temperature. Continuous energy addition gradually induces natural

convective motion in the domain, along with the development of a superheated liquid layer on the heater surface. A minuscule bubble appears slightly before $t^* = 33.3$, marking that as the instant of first nucleation. As the energy injection is continued, the bubble grows in size, increasing the contact area. A significantly larger bubble is visible at $t^* = 41.1$. The expansion of the interface also forces the liquid away from the heated surface, inducing some liquid motion, as is evident from the small velocity vectors appearing around the bubble. Being proportional to the bubble volume, the buoyancy force rapidly enhances with such bulging and attempts to tear the bubble away from the surface, confronting the surface tension force, which is reciprocal to the length of the contact line. The size of the bubble at the instant of departure is decided by the interplay of these two forces. The snapshot corresponding to $t^* = 51.1$ displays the domain immediately after the departure of the first bubble, where a small vapor embryo is left behind, which can expedite the appearance of the next one. The void left by the departure creates a low-pressure zone, and surrounding liquid rushes in to fill that up, as demonstrated by noticeably large velocity vectors. It is, therefore, very much evident that the present algorithm is able to emulate the entire ebullition cycle for the selected configuration.
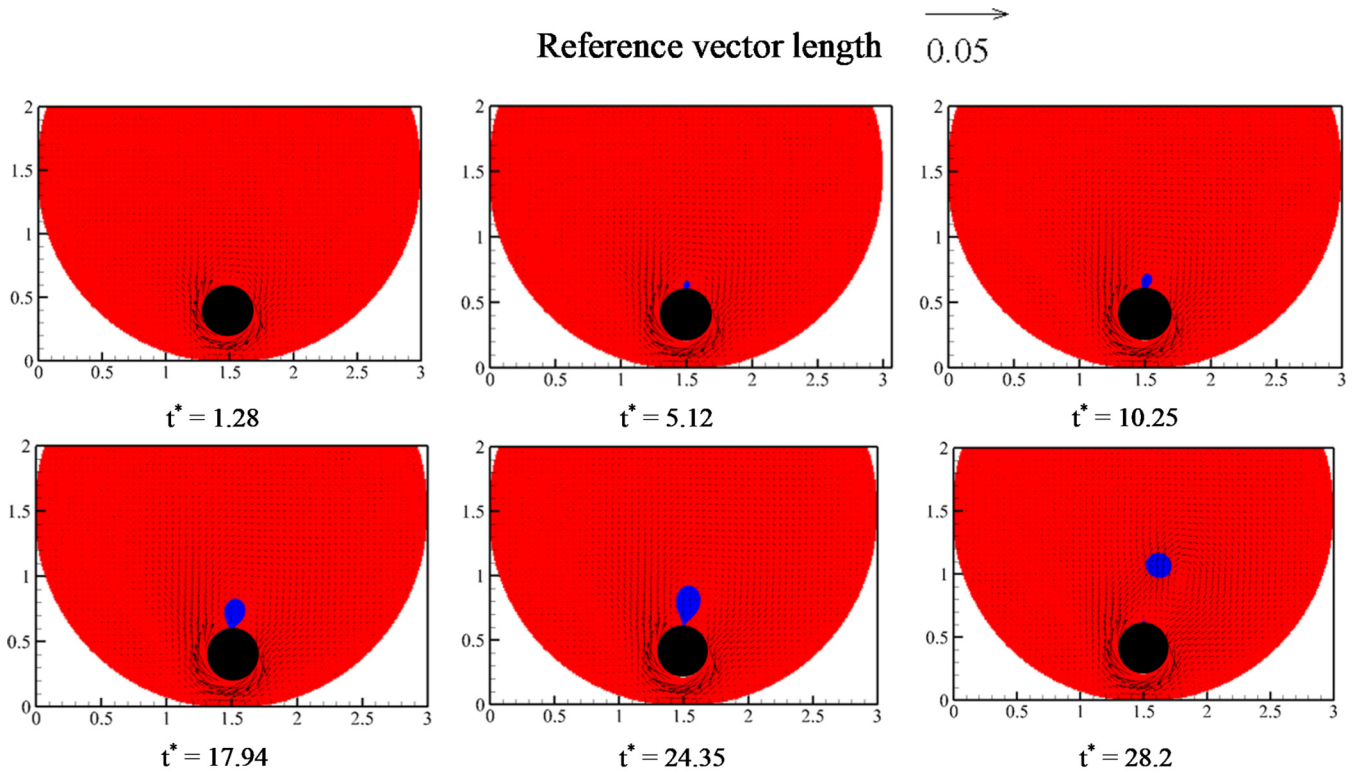
FIG. 7. Snapshots of one bubble ebullition cycle from a microheater in an open cylindrical domain presenting velocity vectors and phase contour; here red and blue colors, respectively, symbolize liquid and vapor phases.

A correlation was proposed by Fritz [45] to identify an analytical expression for bubble departure diameter from a balance between surface tension and buoyancy, which is of the following form:

$$D_d = 0.0208 \sqrt{\frac{\sigma}{g(\rho_l - \rho_v)}} = 0.0208 \, l_0. \qquad (27)$$

Variation in thermophysical properties can be neglected within such a pool because of inconsequential change in the hydrostatic head. Consequently, the departure diameter can be viewed to be inversely proportional to the gravitational acceleration ($D_d \propto g^{-0.5}$), which is a widely used medium for code validation within the LB community [18,20,21,46]. Concerned predictions from our paper are available in Fig. 6(b) for $T_R = 0.75$, demonstrating a very reasonable prediction with an exponent of 0.47, which can be considered to be an indirect validation for the present algorithm. A comparison is also drawn here with scheme A, which predicts an exponent value of 0.45 with identical sets of operating conditions, thereby substantiating the superiority of scheme B over itself.

The temporal variation in heat flux at the nucleation site for two different wall superheat values are presented in Fig. 6(c). A periodic pattern is quite evident, with the heat flux attaining the peak at the moment of bubble departure. The residual embryo promptly starts expanding on the surface, pushing the liquid away from it. Thermal conductivity of vapor being significantly lower than liquid, a drastic plunge in heat flux results, and this phenomenon is referred as *dewetting*. Once the vapor grows reasonably in size, the necking process is initiated, with swift decrease in the vapor-solid contact area and liquid rushing in to fill the void. Heat flux noticeably

increases during such *rewetting*, reaching the maxima on departure, followed by another dewetting and hence completing one ebullition cycle. A larger wall superheat imparts a greater amount of energy into the fluid domain and hence escalates the departure process by reducing the time period of ebullition. Raising the superheat from 0.55 to 0.65 nearly doubles the frequency, with substantial rise ($\approx$19%) in the peak heat flux as well.

E. Cylindrical domain with a microheater

Our next focus is on analyzing the nucleation characteristics in a non-grid-aligned geometry and consequently the fluid domain bounded by two non-co-axial cylinders is selected, the schematic of which is available in Fig. 5(b). Here the inner cylinder is assumed to be rotating in clockwise direction, imposing motion to the initially stagnant fluid. A wall superheat (ΔT_{sup}) of 0.55 is imposed on the microheater surface and prospective developments in the flow domain are presented through a series of snapshots in Fig. 7. The first instant corresponds to $t^* = 1.28$, where no vapor nucleus is present, while the fluid adjacent to the smaller cylinder follows its motion. Such forced flow, however, remains restricted only within a narrow zone around the inner cylinder, with the bulk exhibiting negligible velocity. The first instance of nucleation appears at $t^* = 5.12$, as a small vapor nucleus is visible on the heater surface. Because of the inflicted motion of the neighboring fluid layer, the bubble is pushed in the clockwise direction, emanating asymmetry to the liquid-vapor interface, with the vertical axis increasingly tilting right with time. Subsequent growth of the vapor nucleus is depicted in

the next three snapshots, along with gradual rightward inclination. With rise in bubble size, buoyancy and liquid inertia progressively become stronger in comparison to surface tension, and the necking process is initiated. A very thin neck can be seen around $t^* = 24.35$, signifying that the bubble is about to depart. The bubble rises quickly postdeparture, driven by buoyancy, and also gets pushed further right by the moving liquid ($t^* = 28.2$). A small vapor embryo can be on the heater surface, which leads to the next nucleation, an observation similar to the rectangular domain. The present algorithm can, therefore, claim to have successfully reproduced the ebullition cycle even in cylindrical configuration, despite a staircase representation of the curved surface.

F. Boiling regimes with a distributed heater

With the presence of multiple nucleation sites in the form of a distributed heater, it is possible to identify two distinct regimes of pool boiling [1,21], namely, nucleate and film boiling, separated by a span of transition. Nucleate boiling is characterized by periodic growth of isolated bubbles in distinct nucleation sites at low wall superheat. With rise in wall temperature, such bubbles can merge in the vertical direction, resembling a columnar structure. That causes a sharp ascent in surface heat flux during temperature-controlled experiment and also hinders the movement of liquid rushing in to fill the void, helping the nucleating bubble to grow larger. The number of active nucleation sites also increases with the wall superheat, the consequence of which is the merging of bubbles along the surface and subsequent development of a vapor film. Stable film boiling is feasible only at substantially high wall superheat, where radiation is a major contributor towards overall heat transfer and poor conductivity of vapor limits the conduction counterpart. The transition regime is symbolized by wavering between bubble nucleation and unstable film formation in a nonregular manner, showing glimpses of both the regimes.

While a conventional finite-volume simulation requires the assumption of single or multiple vapor embryos to instigate the numerical procedure [47], Li *et al.* [21] have shown that the LB multiphase model can produce all three modes of pool boiling without any such precondition. So our next objective is to illustrate different regimes of pool boiling using the third geometric orientation described in Sec. IV C, and the observations with three representative wall superheat values are detailed below.

Figure 8 shows the snapshots for four different time instants with a wall superheat of 0.21. The first set of nucleation appears slightly before $t^* = 23.07$, with two sites getting activated close to either edge of the heater. While both these embryos grow into larger bubbles and necking gets initiated, presence of the superheated liquid layer on the heater surface is quite prominent. Both the antecedent bubbles depart around $t^* = 32.04$, leaving a respective minuscule embryo on the surface. Similar to the point heater, departure of the vapor bubble induces substantial liquid motion, which introduces an additional inertial effect into the domain. The departed bubbles approach spherical shape while rising (not shown), which is an indicator of the dominance of the surface tension over inertial force, owing to the smaller velocity level involved

here. This particular pattern of vapor nucleation, growth, and departure is repeated in a periodic sequence, with new nucleation sites getting activated over time around the heater center. Still, for the imposed wall superheat, the number of active nucleation sites remains low enough to restrict the dynamics to the isolated bubble rising mode of the nucleate boiling regime.

The local heat flux, with specified degree of wall superheat, is reliant on the thermal conductivity of the no-slip layer in contact with the heater surface. As the composition of that layer teeters between liquid and vapor, with massive disparity among their respective thermal conductivities, instantaneous area-averaged heat flux is strongly dependent on the relative fraction of heater surface being covered by the vapor phase ($A_f = A_{\text{vapor}}/A_{\text{heater}}$), and can be defined as

$$\dot{q}'' = -\frac{1}{L_H} \int_{-L_H/2}^{+L_H/2} k \frac{\partial T_R}{\partial y}\bigg|_{y=0} dx. \tag{28}$$

Temporal variations in both these parameters are presented in Fig. 8(b), where the span is selected after the first set of nucleation and domain attaining periodicity. It must also be noted that, for a two-dimensional domain, the dimension normal to the plane of the figure can be assumed to be unity, and hence $A_{\text{bubble}} = L_h$. The visual pattern of heat flux ($\dot{q}''$) alteration is quite similar to Fig. 6(c). The heat flux also shows an inverse relationship with the area fraction covered by vapor (A_f), which is very much logical considering the ratio of liquid-to-vapor thermal conductivity $k_l/k_v = 10.1$ for the selected conditions.

A noticeable change in the domain thermal hydraulics can be observed on increasing the wall superheat to 0.27, as demonstrated in Fig. 9. A larger temperature differential at the heater surface infuses energy to the fluid domain at a faster rate, inducing earlier nucleation, despite initial conditions being the same. At $t^* = 10.25$, the heater surface is partially covered by a thin vapor film, owing to the faster rate of vapor generation and merging of neighboring nuclei along the surface, with two prominent bubbles protruding from either ends of the film. These bubbles gradually attain their respective critical volumes because of the continuous energy addition and repudiate the surface to rise upwards ($t^* = 14.09$). It is interesting to observe the oblate shape of these bubbles during their upsurge, which hints towards a balance between inertial and surface tension forces. Compared to the previous case, here the liquid velocity level around the upsurging bubble is noticeably greater, enhancing the inertial effects. Another set of bubbles can be observed over the next two snapshots. Periodic growth and departure of bubbles destabilizes the film, which remains to be capricious and discontinuous. The fraction of heater surface shrouded by the vapor film frequently changes without following any pattern, which is the primary attribute of the transition regime of pool boiling, displaying traits of both nucleate and film boiling simultaneously. The fickle nature of the phenomenon is clearly evident following the irregular appearance of spikes and dips from Fig. 9(b). Any peak in surface heat flux corresponds to a trough in the vapor area fraction, indicating a shrink in the length of vapor film. Such erratic fluctuations are consistent with the observations from Li *et al.* [21], authorizing the transitory nature
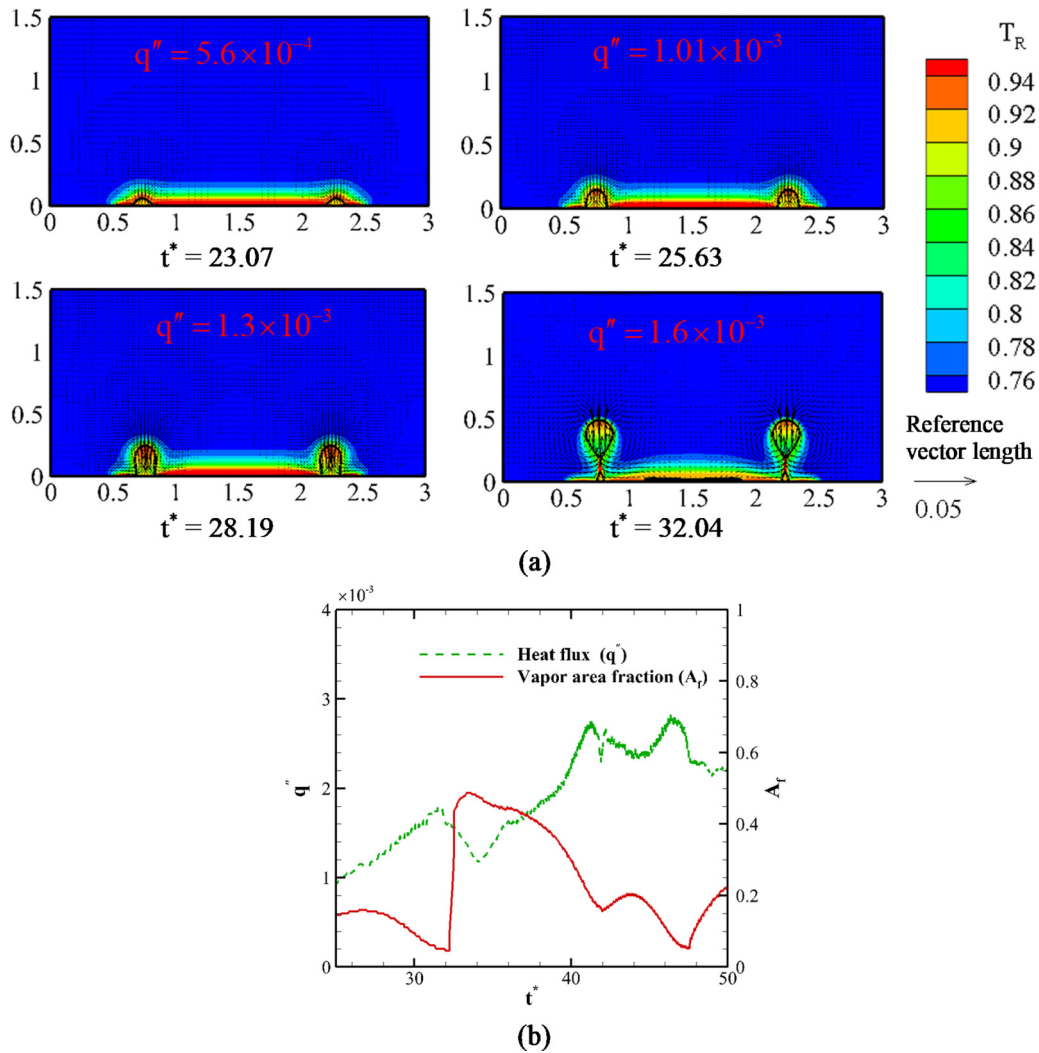
FIG. 8. Characterization of nucleate boiling from a distributed plain heater in an open rectangular domain with $\Delta T_{\text{sup}} = 0.21$: (a) snapshots of bubble nucleation and growth from discrete nucleation sites, where existence of the superheated liquid layer and bubble-induced liquid motion can clearly be seen, and (b) temporal variations in wall heat flux and vapor area fraction, showing considerable rise in heat transmission following departure of a bubble.

of the flow regime. Still the fraction of surface covered by vapor is significantly larger compared to pure nucleate boiling, which is the consequence of the formation of an unstable film.

A more stable vapor film is established with even higher wall superheats, as can be seen from Fig. 10 for $\Delta T_{\text{sup}} = 0.31$. The film covers the entire heater surface, preventing liquid from coming in contact with the heater surface and hence any direct energy addition. The only possible way for the liquid to acquire energy is via conduction through the vapor film, which is naturally a weak process. The thin vapor film present in the first snapshot grows significantly by $t^* = 6.4$, with the primary mode of phase conversion being evaporation at the liquid-vapor interface and subsequent diffusion of molecules across it. With increase in thickness, growth of two vapor bubbles can be seen around $t^* = 10.25$, which leaves the film in the next snapshot. Gradual thickening of the film and thermal convection in liquid in the vicinity of the film introduces substantially larger velocity on the liquid side of the interface. Corresponding shearing action may be

the reason behind ripping off of bubbles from the interface. However, the degree of superheat not being very high, the role of viscosity cannot be ignored either. Accordingly, we are presently not in a position to categorize the vapor formation from the film as a Rayleigh-Taylor instability, originating because of the presence of lighter phase below the heavier one, or Taylor-Helmholtz instability induced by velocity shear [48–50], which demands more focused exploration. In fact, that is not the objective of the present work as well. While the thickness of the film changes with time, it continues to be stable over the heater surface, as it is being substantiated by the magnitude of area fraction (A_f) steadily hovering around 1. The heat flux also constantly persisted with a level much lower than nucleate boiling, compatible with the poor thermal conductivity of vapor.

In conventional multiphase simulations, it is customary to assume the saturation temperature to prevail interior to the bubbles, which is in contrast to the experimental knowledge. The microthermocouple measurement of Wagner and Stephan [51] revealed significant super-
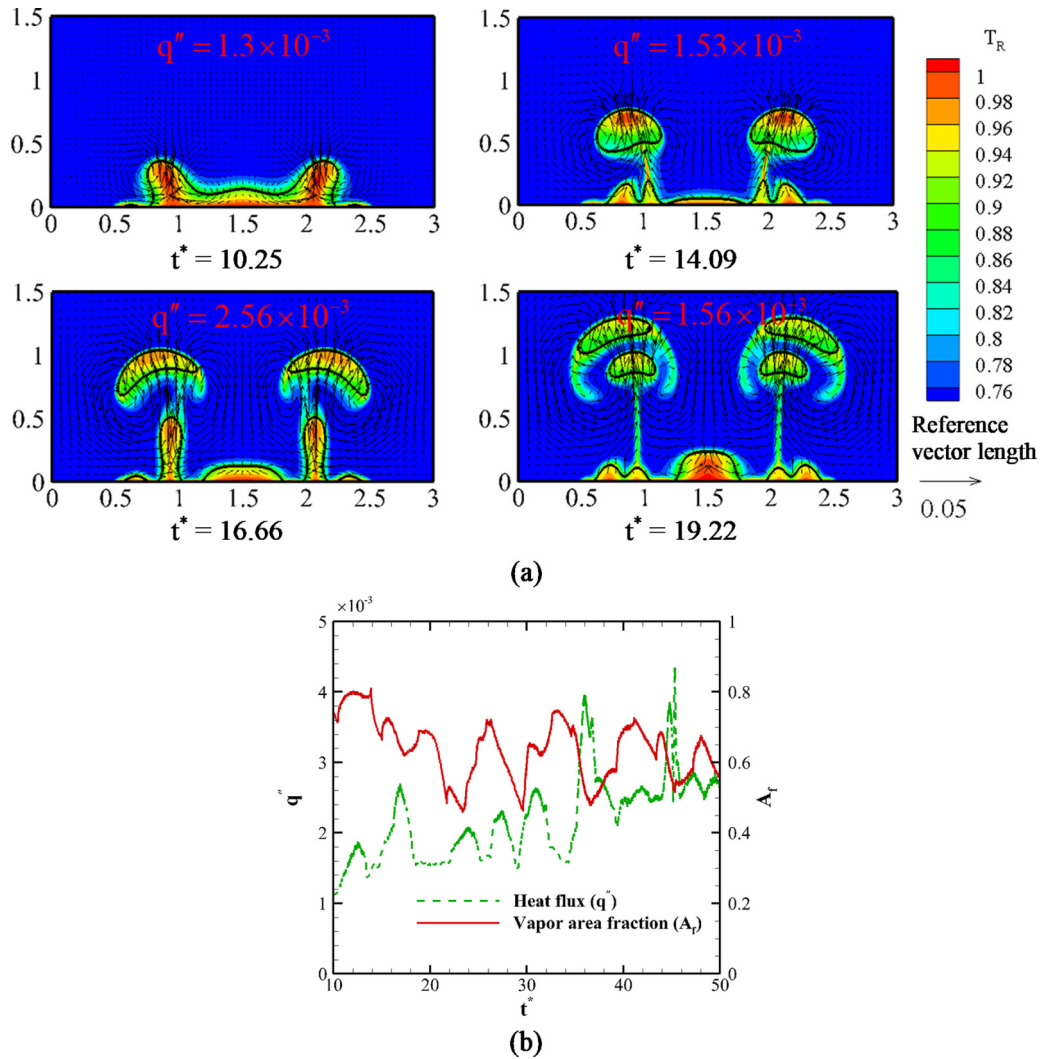
FIG. 9. Characterization of transition boiling from a distributed plain heater in an open rectangular domain with $\Delta T_{\text{sup}} = 0.27$: (a) snapshots of bubble nucleation from an unstable vapor film, the expanse of which keeps on changing with time and the superheated liquid layer of which is also unstable, and (b) temporal variations in wall heat flux and vapor area fraction, signifying the quite chaotic nature of the phenomenon.

heating inside the embryo, which was later reproduced through LB simulations [18,21]. The same has successfully been emulated in the present paper. A substantial temperature gradient exists within the vapor phase, particularly for the ones getting ripped off the film. A thin superheated liquid layer can also be seen around the growing and rising bubbles. So we can claim that the present scheme is competent in capturing both the bubble dynamics and thermofluidic pattern quite realistically.

It is pertinent to mention here that radiation can have a significant role in overall heat transfer during film boiling owing to the rise in absolute surface temperature, and absence of any such model can be recognized as a limitation of our paper. However, the prime objective here is to test the modified discretization scheme for several pool boiling scenarios and the proposed algorithm is definitely successful on that count. Further, the highest absolute surface temperature considered here with R134a is a mere 411.6 K, which is not really high to render radiation significant.

G. Boiling regimes with a structured heater

Appraisal of boiling heat transfer with engineered surfaces is of great practical relevance, as no real surface is perfectly flat in nature and structured surfaces have been reported to enhance the rate of heat transmission [52–55]. There are two possible reasons behind such augmentation in heat transfer. Along with an obvious increase in surface area with columnar structures, thereby directly raising the number of available nucleation sites, the gap between adjacent structures can also house a preexisting nucleus by trapping vapor. The obstructions also induce larger liquid advection, offering a quite dissimilar scenario compared to the plain heater. Therefore, we employ the SC-LBM algorithm with the modified discretization scheme to explore pool boiling with the structured heater shown in Fig. 5(c), and corresponding observations are summarized in Fig. 11 in terms of bubble profiles.

Snapshots presented in Fig. 11(a) refer to the nucleate boiling regime, with distinct bubble generation on different locations of the heater. As mentioned above, the gaps
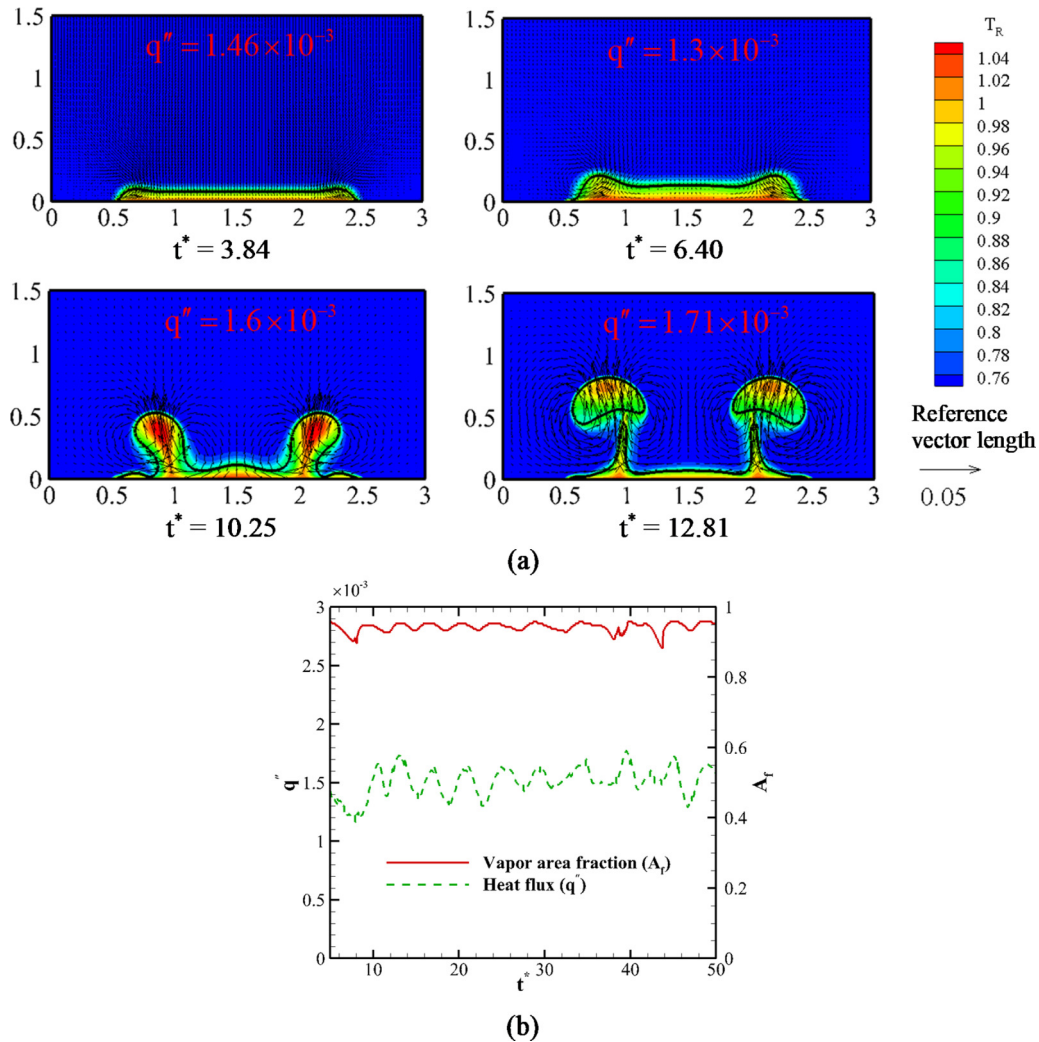
FIG. 10. Characterization of film boiling from a distributed plain heater in an open rectangular domain with $\Delta T_{\text{sup}} = 0.31$: (a) snapshots demonstrating the formation of a stable vapor film over the entire heated surface and occasional vapor release following interfacial instabilities and (b) temporal variations in wall heat flux and vapor area fraction, substantiating the stable nature of the film with the area fraction being near constant around unity.

between the columns act as large rectangular cavities and are always occupied by the vapor phase, therefore consistently providing vapor embryos. The corners of the columns appear to be the most active nucleation site, owing to the structural discontinuity, and embryos appearing on the adjacent corners of neighboring columns can easily merge with each other, producing bigger bubbles. The boiling mechanism from rectangular cavities was explained by Mu *et al.* [19] for a low-density ratio of 10. Despite the density ratio adopted in our paper being about eight times that, the physics remain the same. Significantly higher liquid velocity beneath the departing bubbles has also been noted, which accelerates the upward motion of the bubble.

Transition boiling can be found from Fig. 11(b) for a wall superheat of 0.27. All the structures are covered by vapor film at $t^* = 7.69$, which is definitely not the case at $t^* = 15.38$. A couple of bubbles have already left the surface, completely destroying the film. The film remains unstable over the entire duration of computation. More stable film formation is possible with $\Delta T_{\text{sup}} = 0.31$ [Fig. 11(c)]. Even after the departure of

several bubbles, the film continues to cover the entire heater, affirming the fully developed film boiling regime. The concerned physics is well established and the presented numerical results are consistent with the ones reported by Chang *et al.* [55], albeit for a substantially lower-density ratio of 10. Our modified discretization scheme, therefore, is able to successfully reproduce the pool boiling phenomenon on structured surfaces for higher-density ratios.

H. Boiling curves

As we have already observed, it is possible to experience different regimes of pool boiling with change in wall superheat, with each having its own thermal characteristics. The presence of liquid in contact with the heated surface and enhanced bubble-induced fluid motion steeply increases the wall heat flux during nucleate boiling with rise in superheat. However, for a very high rate of vapor generation leading to the formation of bubble jets, movement of liquid to the heater is hindered, which affects the heat flux and results in
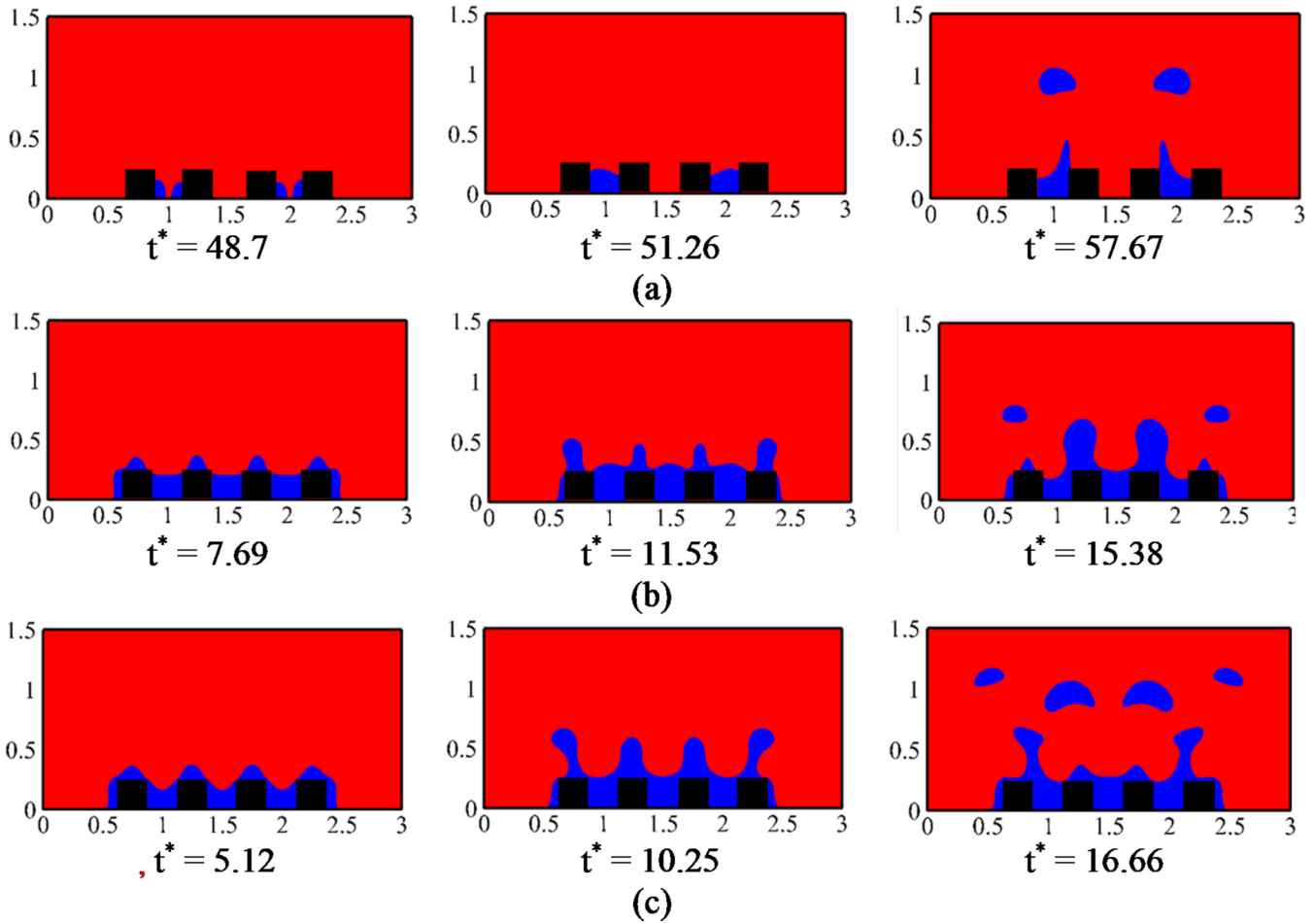
FIG. 11. Snapshots of pool boiling from a distributed plain heater in an open rectangular domain during (a) the nucleate regime with $\Delta T_{\text{sup}} = 0.21$, (b) transition boiling with $\Delta T_{\text{sup}} = 0.27$, and (c) film boiling with $\Delta T_{\text{sup}} = 0.31$. Here red and blue colors, respectively, symbolize liquid and vapor phases. Nucleation can clearly be seen to initiate from the corners of the columnar structures.

a more moderate variation. The number of active nucleation sites also increases with surface temperature, which aids horizontal spreading of the vapor film through merging of bubbles, and consequent evolution to the transient regime. While the vapor area fraction during nucleate boiling remains restricted between 0.1 and 0.5 during the nucleate boiling [Fig. 8(b)], it hovers around 0.7 in the transition regime [Fig. 9(b)] and approaches unity once the film is fully developed. Vapor being a poor thermal conductor, the wall heat flux suffers drastically with such break in thermal communication during film boiling, as has already been observed from Fig. 10(b). After stabilization of the film, however, the heat flux starts climbing again, mostly as a linear function of the degree of superheat.

The above discussion is traditionally conceived in terms of the boiling curve [1] and the same approach is followed in Fig. 12, where we have plotted the time-average wall heat flux against the degree of superheat. Following Ma *et al.* [23], the average flux is defined as

$$\dot{q}''_{\text{avg}} = -\frac{1}{L_H(t_2 - t_1)} \int_{t_1}^{t_2} \int_{-L_H/2}^{+L_H/2} k \frac{\partial T_R}{\partial y}\bigg|_{y=0} dx \quad (29)$$

where $(t_2 - t_1)$ is a very long time interval, which starts after the initiation of vapor generation. The culmination of the

nucleate boiling regime is identified in terms of the critical heat flux (CHF), whereas the onset of film boiling corresponds to the Leidenfrost point. All the three modes of pool boiling, along with the transformation points, have nicely been represented for both plain and structured surfaces. As postulated earlier, the structured surface consistently enjoys greater heat flux for any specified superheat. The CHF value with the structured surface is also noticeably higher, as the peaks of the columns are more likely to remain in contact with the liquid than the plain surface. A higher rate of heat transfer also allows a stable film formation at comparatively lower superheat, thereby shifting the Leidenfrost point to the left and substantially limiting the extent of transition boiling.

A quantitative validation is attempted by allegorizing the CHF predicted for the plain surface with correlations from literature, and the well-known Zuber relation [56] is employed for the same, which has the following form:

$$\dot{q}''_{\text{CHF}} = K h_{fg} \rho_v \left[\frac{\sigma g(\rho_l - \rho_v)}{\rho_v^2} \right]. \quad (30)$$

Sun and Lienhard (from [56]) suggested a value of 0.149 for the constant K, which yields a theoretical CHF value of 2.079×10^{-3} lattice units for R134a with the present domain, whereas our simulation produces an anticipated CHF value of
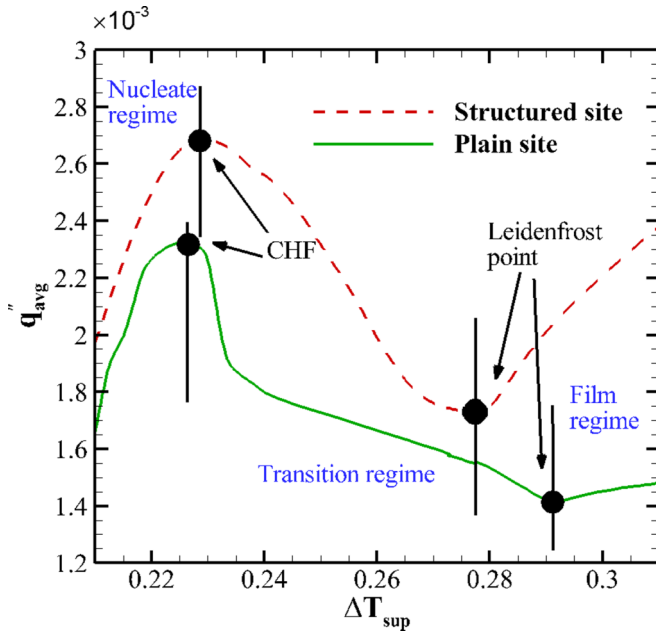
FIG. 12. Boiling curves with plain and structured distributed heaters in an open rectangular domain. The transition regime with the structured heater is noticeably shorter, with CHF getting shifted towards the right and the Leidenfrost point shifted towards the left. The heat flux level with the structured heater is also consistently higher than that with the plain heater, yielding a greater CHF value.

FIG. 13. The static contact angle inversely varies with the false wall density and approaches the theoretical extremes of $0°$ and $180°$ on assuming the limiting density values corresponding to vapor and liquid, respectively, as shown within the insets.

2.33×10^{-3} lattice units, which is within 10% accuracy level, and hence can be considered to be satisfactory.

I. Effect of surface wettability

The numerical approach of incorporating the surface wettability force in our algorithm is one final aspect to be discussed. The false wall density appearing in Eq. (16) is a direct representation of the contact angle effective at the three-phase interface, as can be comprehended from Fig. 13. It is definite that a value of ρ_w closer to liquid density yields a low contact angle, whereas the reverse is true for a value approaching vapor density. A higher contact angle refers to a reduction in surface wettability, which allows the vapor to accumulate over the heated surface more easily, causing a decline in the heat transfer rate and hence a greater penchant towards film boiling. The same can be substantiated from Fig. 14, where two different contact angles have been explored, namely, $39.22°$ and $56.97°$, with the configuration probed earlier in Sec. IV F. It can be seen from the figures that, for the same wall superheat and at the same time instants, the fluid with greater contact angle is able to spread wider over the heater. Variations in vapor area fraction and surface heat flux with time are presented in Fig. 14(c) for the sake of quantification, and that firmly supports our earlier discussion.

The boiling curve is also strongly affected by the contact angle, as is illustrated in Fig. 14(d). Heat transfer rate for a fluid with lower contact angle being relatively higher, the effect of vapor accumulation owing to the vertical merging of bubbl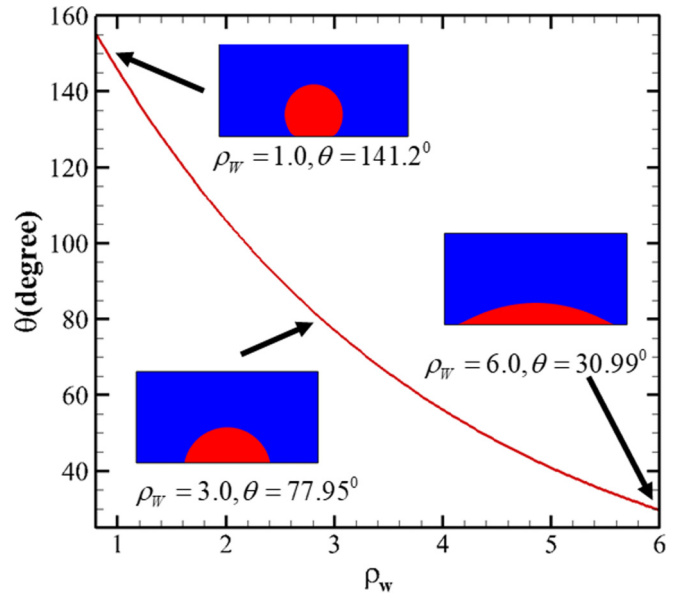es is delayed quite noticeably. Around the point of onset of nucleate boiling, the surface is mostly in contact with the liquid and hence there is no prominent effect of the contact angle on the boiling curves. However, the curves veer from each other with rise in wall superheat. The difference in respective CHF values is quite remarkable, considering the change in selected contact angles is not very large. This particular observation of reduction in CHF with enhancement in contact angle is well documented in literature [57–59]. So we can conclude that the modified discretization scheme is successful in capturing the effect of contact angle and surface wettability on pool boiling.

V. CONCLUSIONS

A detailed discussion regarding the deployment of the pseudopotential-based lattice Boltzmann method for simulation of pool boiling is presented here. While it has received conspicuous recognition in literature over the last couple of decades, inherent thermodynamic inconsistency of the basic algorithm has limited its application to low-density ratios and hence only around the critical point of a fluid. We, therefore, attempt to reinforce the existing approach, through simultaneous enhancement of isotropy of the discrete equation and thermodynamic consistency of the overall formulation, by reshaping the interparticle interaction term and extending its discretization to the eighth order. The immediate consequence of such augmentation can be envisaged following the stabilization of a static liquid droplet in a periodic domain. The proposed algorithm is able to coax about 113% reduction in the largest spurious velocity around the curved interface for comparable density ratios, while sustaining the simulation at a density ratio of 620, which is a substantial improvement over about 174 for the existing schemes. Predicted phasic densities
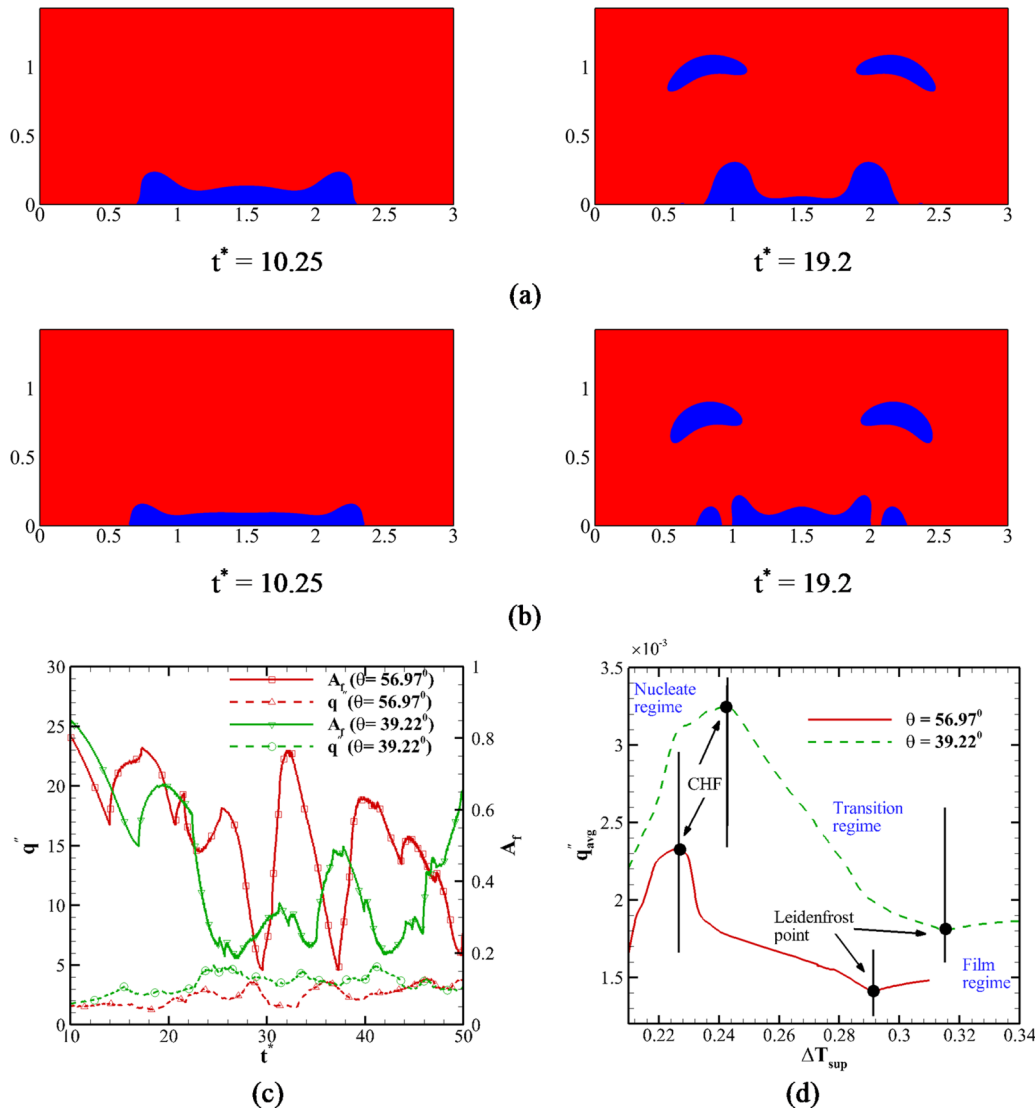
FIG. 14. Effect of contact angle on the nature of bubble nucleation demonstrated for (a) $\theta = 39.22°$ and (b) $\theta = 56.97°$, with red and blue colors, respectively, symbolizing liquid and vapor phases; (c) temporal variations in wall heat flux and vapor area fraction for $\Delta T_{\text{sup}} = 0.25$; and (d) boiling curves for the same contact angles. Fluid with higher contact angle clearly shows a greater inclination towards stable film formation, resulting in a substantial reduction in CHF under identical operating conditions.

also complied well with the Maxwell area reconstruction rule, thereby providing an indirect validation.

Several pool boiling scenarios have been explored to demonstrate the capability of the proposed algorithm. Consistent with earlier SC-LB procedures, it successfully simulates the nucleation on the superheated surface, without necessitating any assumed nucleus. A complete ebullition cycle is produced using a microheater on both rectangular and cylindrical configurations, as well as with distributed planar and structured heater surfaces. All three regimes of pool boiling, namely, nucleate, transition, and film boiling, have been captured with precision, along with their standard characteristics in terms of heat transfer coefficient and vapor area fraction, facilitating the development of a complete boiling curve. The CHF value predicted for the planar heater matches within 10% with the well-celebrated relation of Zuber, which substantiates its proficiency in simulation of pool boiling. To our knowledge, such an attempt of correlating a computational inference with an empirical relation is rare in the LB community, particularly for multiphase models, and that speaks volumes about the diligence of the proposed augmentation in the SRT-SC-LB algorithm.

As has already been mentioned, incorporation of a suitable radiation model is required for precise replication of film boiling for fluids with high critical temperature. Also the adoption of MRT-LBM with proposed augmentation is expected to further expand the range of density ratios, optimistically approaching atmospheric conditions, and hence can be viewed as the next logical step of continued research.

TABLE I. List of coefficients involved in the discretized SC force [26].

Coefficient	γ_1	γ_2	γ_3	γ_4	γ_5	γ_6	γ_7	γ_8
$E^{(4)}$	$1/3$	$1/12$	0	0	0	0	0	0
$E^{(8)}$	$4/21$	$4/45$	0	$1/60$	$2/315$	0	0	$1/5040$

APPENDIX: DISCRETIZED FORCES

As explained by Shan [26], it is never possible to make all the tensorial terms $E^{(n)}$ of Eq. (25) perfectly isotropic in a finite domain, and therefore it is imperative to ensure that the finite difference operator in the discretized form has the highest degree of isotropy. The weights, therefore, need to be optimized to minimize the discretization error. The procedure to evaluate the same to the sixth order was detailed by Wolfram [60], which was later adopted by Shan [26] to expand to $E^{(8)}$. As mentioned in the main text, we are looking for a logical amalgamation of the interparticle interaction force proposed by Gong and Cheng [33], with the multirange discretization [26]. Consequently, the discretized forms of the modified SC force [Eq. (25)] at a particular time instant t in both x and y directions are presented below, while the involved coefficients are summarized in Table I following [26]. Here each ψ refers to the local instantaneous magnitude:

$$
\begin{aligned}
F^{SC}_{x_{i,j}} = &-G_{SC}\beta\psi_{i,j}\Delta t\left[\begin{array}{c} l\gamma_1(\psi_{i+1,j}-\psi_{i-1,j})+\gamma_2(\psi_{i+1,j+1}-\psi_{i-1,j+1}+\psi_{i+1,j-1}-\psi_{i-1,j-1})+2\gamma_4(\psi_{i+2,j}-\psi_{i-2,j}) \\ +\gamma_5\{2(\psi_{i+2,j+1}-\psi_{i-2,j+1}+\psi_{i+2,j-1}-\psi_{i-2,j-1})+\psi_{i+1,j+2}-\psi_{i-1,j+2}+\psi_{i+1,j-2}-\psi_{i-1,j-2}\} \\ +2\gamma_8(\psi_{i+2,j+2}-\psi_{i-2,j+2}+\psi_{i+2,j-2}-\psi_{i-2,j-2}) \end{array}\right] \\
&-G_{SC}\frac{1-\beta}{2}\Delta t\left[\begin{array}{c} l\gamma_1(\psi^2_{i+1,j}-\psi^2_{i-1,j})+\gamma_2(\psi^2_{i+1,j+1}-\psi^2_{i-1,j+1}+\psi^2_{i+1,j-1}-\psi^2_{i-1,j-1})+2\gamma_4(\psi^2_{i+2,j}-\psi^2_{i-2,j}) \\ +\gamma_5\{2(\psi^2_{i+2,j+1}-\psi^2_{i-2,j+1}+\psi^2_{i+2,j-1}-\psi^2_{i-2,j-1})+\psi^2_{i+1,j+2}-\psi^2_{i-1,j+2}+\psi^2_{i+1,j-2}-\psi^2_{i-1,j-2}\} \\ +2\gamma_8(\psi^2_{i+2,j+2}-\psi^2_{i-2,j+2}+\psi^2_{i+2,j-2}-\psi^2_{i-2,j-2}) \end{array}\right],
\end{aligned}
\tag{A1}
$$

$$
\begin{aligned}
F^{SC}_{y_{i,j}} = &-G_{SC}\beta\psi_{i,j}\Delta t\left[\begin{array}{c} l\gamma_1(\psi_{i,j+1}-\psi_{i,j-1})+\gamma_2(\psi_{i+1,j+1}-\psi_{i+1,j-1}+\psi_{i-1,j+1}-\psi_{i-1,j-1})+2\gamma_4(\psi_{i,j+2}-\psi_{i,j-2}) \\ +\gamma_5\{2(\psi_{i+2,j+1}-\psi_{i+2,j-1}+\psi_{i-2,j+1}-\psi_{i-2,j-1})+\psi_{i+1,j+2}-\psi_{i+1,j-2}+\psi_{i-1,j+2}-\psi_{i-1,j-2}\} \\ +2\gamma_8(\psi_{i+2,j+2}-\psi_{i+2,j-2}+\psi_{i-2,j+2}-\psi_{i-2,j+2}) \end{array}\right] \\
&-G_{SC}\frac{1-\beta}{2}\Delta t\left[\begin{array}{c} l\gamma_1(\psi^2_{i,j+1}-\psi^2_{i,j-1})+\gamma_2(\psi^2_{i+1,j+1}-\psi^2_{i+1,j-1}+\psi^2_{i-1,j+1}-\psi^2_{i-1,j-1})+2\gamma_4(\psi^2_{i,j+2}-\psi^2_{i,j-2}) \\ +\gamma_5\{2(\psi^2_{i+2,j+1}-\psi^2_{i+2,j-1}+\psi^2_{i-2,j+1}-\psi^2_{i-2,j-1})+\psi^2_{i+1,j+2}-\psi^2_{i+1,j-2}+\psi^2_{i-1,j+2}-\psi^2_{i-1,j-2}\} \\ +2\gamma_8(\psi^2_{i+2,j+2}-\psi^2_{i+2,j-2}+\psi^2_{i-2,j+2}-\psi^2_{i-2,j-2}) \end{array}\right].
\end{aligned}
\tag{A2}
$$

[1] J. G. Collier and J. R. Thome, *Convective Boiling and Condensation*, 3rd ed. (Clarendon, Oxford, 1994).

[2] S. Nukiyama, Int. J. Heat Mass Transf. **27**, 955 (1984).

[3] J. Kim, Int. J. Multiphase Flow **35**, 1067 (2009).

[4] V. K. Dhir, G. R. Warrier, and E. Aktinol, J. Heat Transfer **135**, 061502 (2013).

[5] G. Son and V. Dhir, J. Heat Transfer **119**, 525 (1997).

[6] S. W. Welch and J. Wilson, J. Comput. Phys. **160**, 662 (2000).

[7] D. Sun and W. Tao, Int. J. Heat Mass Transf. **53**, 645 (2010).

[8] V. Pandey, G. Biswas, A. Dalal, and S. W. Welch, J. Heat Transfer **140**, 121503 (2018).

[9] T. Krüger, H. Kusumaatmaja, A. Kuzmin, O. Shardt, G. Silva, and E. Viggen, *The Lattice Boltzmann Method: Principles and Practice* (Springer-Verlag, Berlin, 2016).

[10] H. Huang, M. C. Sukop, and X. Lu, *Multiphase Lattice Boltzmann Methods: Theory and Application* (Wiley, New York, 2015).

[11] M. R. Swift, W. R. Osborn, and J. M. Yeomans, Phys. Rev. Lett. **75**, 830 (1995).

[12] X. Shan and H. Chen, Phys. Rev. E **47**, 1815 (1993).

[13] X. Shan and H. Chen, Phys. Rev. E **49**, 2941 (1994).

[14] X. Shan and G. Doolen, J. Stat. Phys. **81**, 379 (1995).

[15] X. Shan, Phys. Rev. E **77**, 066702 (2008).

[16] A. Márkus and G. Házi, Phys. Fluids **20**, 022101 (2008).

[17] S. Gong and P. Cheng, Int. J. Heat Mass Transf. **55**, 4923 (2012).

[18] S. Gong and P. Cheng, Int. J. Heat Mass Transf. **64**, 122 (2013).

[19] Y.-T. Mu, L. Chen, Y.-L. He, Q.-J. Kang, and W.-Q. Tao, Int. J. Heat Mass Transf. **106**, 708 (2017).

[20] W.-Z. Fang, L. Chen, Q.-J. Kang, and W.-Q. Tao, Int. J. Therm. Sci. **114**, 172 (2017).

[21] Q. Li, Q. Kang, M. M. Francois, Y. He, and K. Luo, Int. J. Heat Mass Transf. **85**, 787 (2015).

[22] S. Gong and P. Cheng, Int. J. Heat Mass Transf. **85**, 635 (2015).

[23] X. Ma, P. Cheng, S. Gong, and X. Quan, Int. J. Heat Mass Transf. **114**, 453 (2017).

[24] Q. Li, Y. Yu, P. Zhou, and H. Yan, Appl. Therm. Eng. **132**, 490 (2018).

[25] C. Zhang and P. Cheng, Int. J. Heat Mass Transf. **110**, 319 (2017).

[26] X. Shan, Phys. Rev. E **73**, 047701 (2006).

[27] A. J. Wagner, Int. J. Mod. Phys. B **17**, 193 (2003).

[28] X. He, S. Chen, and R. Zhang, J. Comput. Phys. **152**, 642 (1999).

[29] M. Mohammadi-Shad and T. Lee, Phys. Rev. E **96**, 013306 (2017).

[30] T. Seta and K. Okui, J. Therm. Sci. Technol. **1**, 125 (2006).

[31] Y. Tanaka, M. Yoshino, and T. Hirata, Commun. Comput. Phys. **9**, 1347 (2011).

[32] L. Fei, J. Yang, Y. Chen, H. Mo, and K. H. Luo, Phys. Fluids **32**, 103312 (2020).

[33] S. Gong and P. Cheng, Comput. Fluids **53**, 93 (2012).

[34] P. L. Bhatnagar, E. P. Gross, and M. Krook, Phys. Rev. **94**, 511 (1954).

[35] A. Kupershtokh and D. Medvedev, J. Electrost. **64**, 581 (2006).

[36] Q. Kang, D. Zhang, and S. Chen, Phys. Fluids **14**, 3203 (2002).

[37] P. Yuan and L. Schaefer, Phys. Fluids **18**, 042101 (2006).

[38] D.-Y. Peng and D. B. Robinson, Ind. Eng. Chem. Fundam. **15**, 59 (1976).

[39] A. Kupershtokh, D. Medvedev, and D. Karpov, Comput. Math. Appl. **58**, 965 (2009).

[40] R. Benzi, L. Biferale, M. Sbragaglia, S. Succi, and F. Toschi, Phys. Rev. E **74**, 021509 (2006).

[41] G. Házi and A. Márkus, Int. J. Heat Mass Transf. **52**, 1472 (2009).

[42] M. Sbragaglia, R. Benzi, L. Biferale, S. Succi, K. Sugiyama, and F. Toschi, Phys. Rev. E **75**, 026702 (2007).

[43] A. Kuzmin, A. Mohamad, and S. Succi, Int. J. Mod. Phys. C **19**, 875 (2008).

[44] Q. Li, K. H. Luo, and X. J. Li, Phys. Rev. E **87**, 053301 (2013).

[45] W. Fritz, Phys. Z. **36**, 379 (1935).

[46] S. Gong and P. Cheng, Numer. Heat Transfer, Part A **65**, 644 (2014).

[47] D. Garg and V. Dhir, J. Heat Transfer **141**, 011504 (2019).

[48] C. H. Panzarella, S. H. Davis, and S. G. Bankoff, J. Fluid Mech. **402**, 163 (2000).

[49] G. Tomar, G. Biswas, A. Sharma, and S. Welch, Phys. Fluids **20**, 092101 (2008).

[50] A. Hens, G. Biswas, and S. De, Phys. Fluids **26**, 012105 (2014).

[51] E. Wagner and P. Stephan, J. Heat Transfer **131**, 121008 (2009).

[52] J. Wei, L. Guo, and H. Honda, Heat Mass Transfer **41**, 744 (2005).

[53] D. Cooke and S. G. Kandlikar, J. Heat Transfer **133**, 052902 (2011).

[54] K.-H. Chu, R. Enright, and E. N. Wang, Appl. Phys. Lett. **100**, 241603 (2012).

[55] X. Chang, H. Huang, Y.-P. Cheng, and X.-Y. Lu, Int. J. Heat Mass Transf. **139**, 588 (2019).

[56] S. M. Ghiaasiaan, *Two-Phase Flow, Boiling, and Condensation: In Conventional and Miniature Systems* (Cambridge University, Cambridge, England, 2007).

[57] S. G. Kandlikar, J. Heat Transfer **123**, 1071 (2001).

[58] Y. Takata, S. Hidaka, J. Cao, T. Nakamura, H. Yamamoto, M. Masuda, and T. Ito, Energy **30**, 209 (2005).

[59] R. Chen, M.-C. Lu, V. Srinivasan, Z. Wang, H. H. Cho, and A. Majumdar, Nano Lett. **9**, 548 (2009).

[60] S. Wolfram, J. Stat. Phys. **45**, 471 (1986).